A 100-m-Scale Modeling Study of a Gale Event on the Lee Side of a Long Narrow Mountain

Haile Xue and Jian Li

State Key Laboratory of Severe Weather, Chinese Academy of Meteorological Sciences, Beijing, China

Tingting Qian

State Key Laboratory of Severe Weather, and Institute of Tibetan Plateau and Polar Meteorology, Chinese Academy of Meteorological Sciences, Beijing, China

Hongping Gu

Utah Climate Center, Utah State University, Logan, Utah

(Manuscript received 22 March 2019, in final form 18 October 2019)

ABSTRACT

In this study, a gale event that occurred on the lee side of a long narrow mountain was investigated, together with the associated mountain flows, using a realistic-case large-eddy simulation (LES) that is based on the Weather Research and Forecasting Model. The mountain is located on the southeastern Tibetan Plateau, where approximately 58 gales occur annually, mostly in the afternoons during the winter season. Benefitting from realistic topography and high horizontal resolution as fine as 111 m, the LES can replicate features similar to the wind fields observed during the gale period. Investigation of the early morning wind structure over the mountain revealed that weak inflows were blocked, reversed, and divided in the upstream area and that some weak lee waves, rotors, and two clear lee vortices were evident downstream. As the upstream wind accelerated and the boundary layer developed during the daytime, the lee waves became amplified with severe downslope wind and rotors. The interaction and coherent structure of the downslope wind, rotor, and vortices were investigated to show the severe wind distribution. The mountain drags associated with blocking and amplified lee waves are displayed to show the potential impact on the large-scale model. The linear lee-wave theory was adopted to explain the wave evolution during this event together with a discussion of the uncertainty around low-level nonlinear processes.

1. Introduction

Severe winds on the lee side of mountains, known as downslope windstorms, have been observed and studied in many areas, for example, Boulder, Colorado, on the eastern slopes of the Rocky Mountains and in the lee of Medicine Bow in Wyoming (Brinkmann 1974; Pokharel et al. 2017), the northern slopes of the Alps in Europe (Jiang and Doyle 2004; Smith et al. 2007), and the eastern Adriatic coast (Grisogono and Belusic 2009). Such examples of downslope windstorms are associated with substantial topographic features with

long horizontal wavelengths (i.e., ~100 km). Downslope windstorms can also be observed in association with more modest topography (wavelength: ~20–30 km), for example, High Point in New Jersey (Decker and Robinson 2011), the Falkland Islands (Mobbs et al. 2005; Sheridan and Vosper 2006), and Iceland (Ólafsson and Ágústsson 2007; Rögnvaldsson et al. 2011). Some windstorms can even be observed in the valleys between 2-km-scale hills over northern Norway (Grønås and Sandvik 1999). These downslope windstorms indicate that a strong interaction can occur between the local mountain and upper atmosphere over a wide spectrum of topography. The multiscale topographies on the Tibetan Plateau have a high impact on the regional and global weather and climate (Shi et al. 2008; Boos and Kuang 2010; Shi et al. 2017; Zhao et al. 2018). The precipitation bias over orographic regions,

especially over the Tibetan Plateau, is higher than in other regions due to the multiple model evaluations (Phillips and Gleckler 2006). The mountain flow dynamics and their influence in area around Tibetan Plateau were not studied in depth, mainly due to the deficiency in fine observations. Fortunately, there are some observations available over and around the targeted mountain, Cang Mountain (CM), although the available data are not adequate to independently resolve the mountain flows, which are already quite fine compared to other regions on the Tibetan Plateau. The CM, which is a typical mountain in this region, has a north-northwest–south-southeast orientation and forms an approximately 2D ridge with a length of ~45 km and a width varying from 12 to 20 km from south to north (Figs. 1b,d). Gales are frequently observed on the lee side of this mountain (Yang et al. 2013), which indicates severe mountain flows may exist in the area. In this case study, we attempt to combine the existing observations with a realistic large-eddy simulation (LES) to investigate the diurnal evolution of mountain flows and mountain waves and the impacts on the low-level downstream flow interaction and mountain drag that are important in large-scale models to fill the gap of mountain flow studies on the Tibetan Plateau.

Severe downslope winds are generally related to mountain waves (Scorer and Klieforth 1959; Durran 1986, 1990; Smith et al. 2007), and among such waves, lee waves that are trapped in the lower troposphere generally have wavelengths on the order of 5–10 km (Sawyer 1960). Therefore, the simulation of lee waves requires a horizontal resolution of at least 1 km (Li and Chen 2017; Udina et al. 2017). In addition, models require high resolution to resolve both the realistic topography and the associated small-scale atmospheric processes. The properties (amplitude and wavelength) of lee waves are considerably influenced by mountain parameters and planetary boundary layer (PBL) processes (Pearce and White 1967; Jiang et al. 2006; Smith 2007; Wang et al. 2010; Li and Chen 2017). The PBL parameterization schemes in mesoscale numerical models are problematic with regard to the simulation of a stable boundary layer; that is, the schemes tend to result in more vertical mixing in the presence of synoptic flow above a stable boundary layer and less vertical mixing during calm periods at night (Teixeira et al. 2008; Baklanov et al. 2011; Shin and Hong 2011; Holtslag et al. 2013). In comparison, LESs are more accurate at capturing turbulent interactions between a stable boundary layer and flow aloft (Crosman and Horel 2017).

Trapped lee waves have been simulated using the Weather Research and Forecasting (WRF) Model with a 1-km horizontal resolution in recent studies (Li and Chen 2017; Udina et al. 2017). Udina et al. (2017) found that a 1-km-resolution model was able to reproduce lee waves, except that their wavelengths were underestimated in comparison with satellite-based observations, which may have been attributable to underestimation of the upstream wind speed. Furthermore, their simulations were also unable to capture mountain-induced small-scale flows, for example, blocking flows and rotors. Udina et al. (2017) suggested that LESs should be utilized to investigate the interaction between waves and the PBL to clarify the details of mountain-induced-flow processes.

In an LES, resolved and turbulent motions are separated using a physical length scale, which is advantageous for studies of turbulent flows (Chow et al. 2005). In several previous studies, realistic-case LESs have been performed for certain phenomena, for example, thermally induced slope-wind/valley-wind systems (Chow et al. 2006), hurricane boundary layer rolls (Zhu 2008), microscale weather flows for wind energy applications (Liu et al. 2011), and nighttime flow dynamics during stable conditions in California's Owens Valley (Zhou and Chow 2013). More recently, Muñoz-Esparza et al. (2017) performed a WRF-nested realistic LES of a diurnal cycle. Their results showed a good match between the simulation and field campaign observations as the horizontal grid size is small as 8 m (32 m) for stable (convective) PBL. The night global intermittency features in a stable PBL have been reproduced (Muñoz-Esparza et al. 2017). Van Stratum and Stevens (2015) showed that the consequence of misrepresenting nighttime ABL turbulence on daytime convection is small. In addition, a relative coarse-resolution (250-m grid spacing) LES, conducted to simulate the cold-air pool Salt Lake Valley, shows that the overall depth and vertical temperature gradient of the cold-air pool are more realistically modeled by WRF and LES than the WRF mesoscale simulation (Crosman and Horel 2017). These studies have indicated that the LES is capable of capturing the microscale flow features, stable flows, and vertical structure of the atmosphere. However, to the best of our knowledge, a realistic-case LES configuration has not been applied to the investigation of severe lee winds.

In this study, existing observations were combined with a realistic LES (111-m horizontal grid size) to investigate a gale event occurred on the lee side of CM to understand 1) what exactly occurs in the lower and upper troposphere in terms of the mountain flows during the frequently observed gale period on the Tibetan Plateau that may be missed in the mesoscale and large-scale models and 2) how the missed mountain flows influence the environmental atmosphere, which
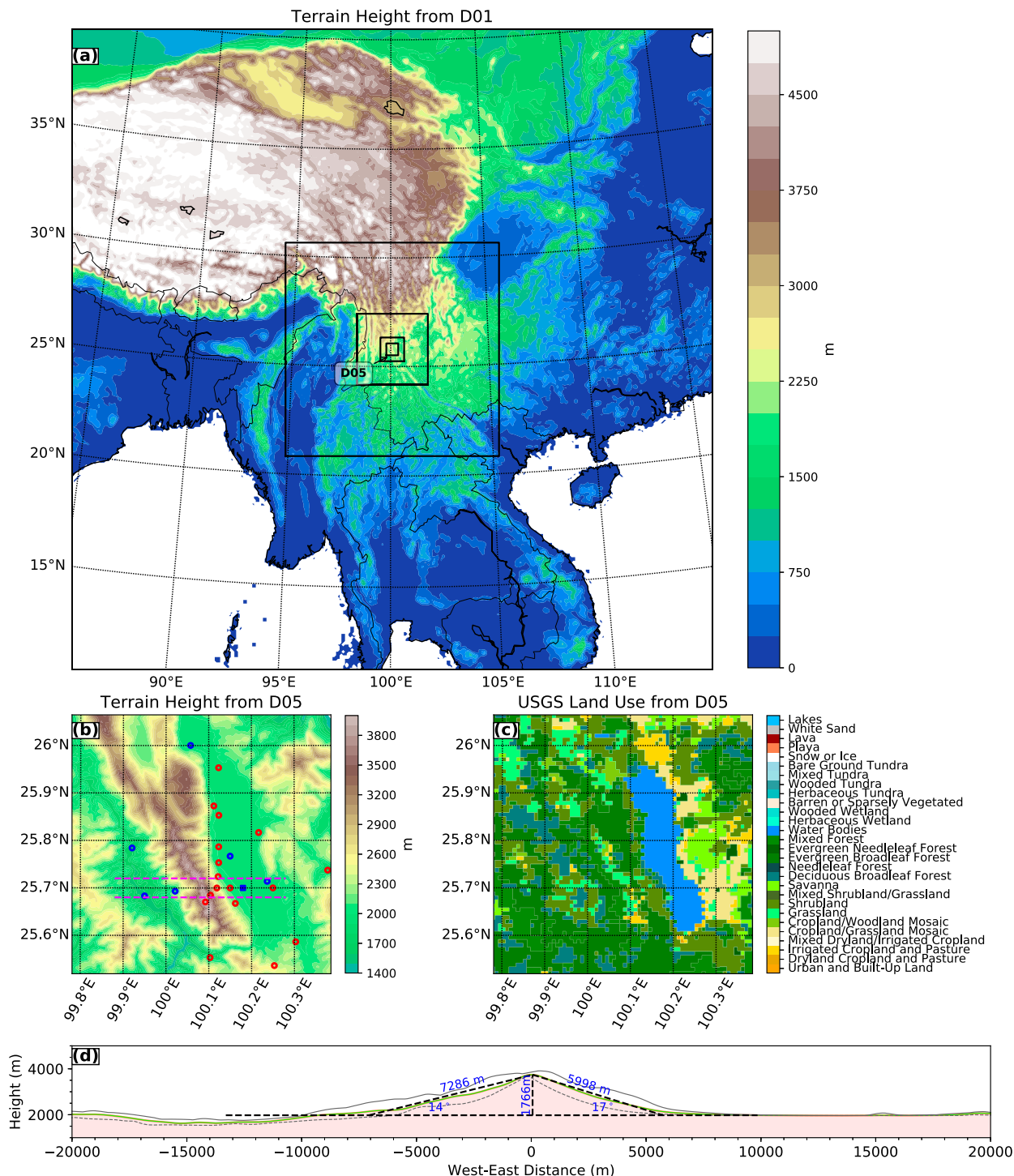
FIG. 1. Terrain height from WRF-nested domains (a) D01 and (b) D05, and (c) U.S. Geological Survey (USGS) land use in WRF domain D05. The black-outlined rectangles show the domains, and the fifth domain is marked as D05 in (a). Blue (10-m wind and 2-m temperature observations available) and red (only 2-m temperature observations available) dots in (b) denote automatic weather stations. The blue square denotes the Dali station where the wind profile radar is located and for which both 2-m temperature and 10-m wind observations are available. (d) Cross section of terrain height. The green line is mean height between the two magenta lines in (b), the solid line is maximum height between the two magenta lines in (b), and the dashed line is minimum height between the two magenta lines in (b). Average slope lengths and angles are depicted with blue characters.
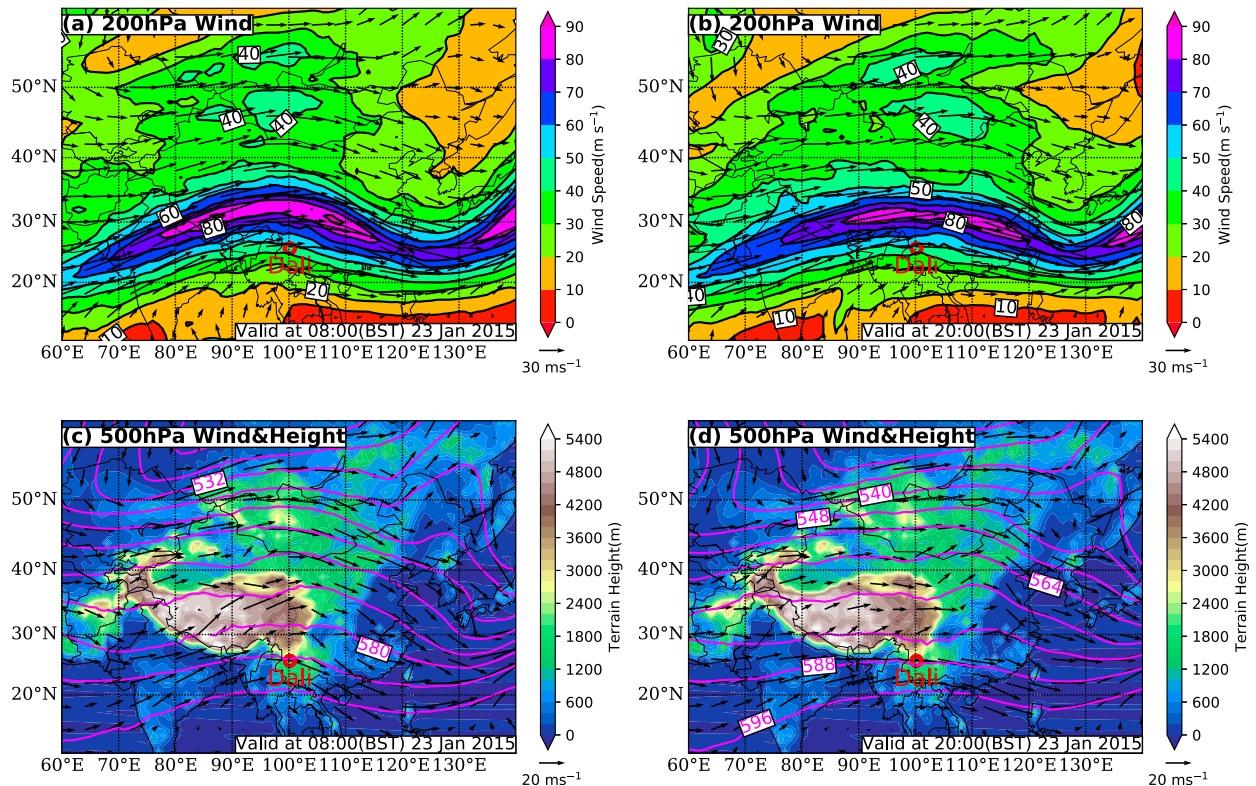
FIG. 2. NCEP-FNL products of (a),(b) 200-hPa wind vector (arrows) and wind speed (m s^{-1}; shading) and (c),(d) 500-hPa geopotential height (gpm; contours), wind vector (arrows), and terrain height (shading) valid at (left) 0800 and (right) 2000 BST 23 Jan 2015.

may provide some potential understanding for the improvement of the orographic parameterization schemes in large-scale models. The remainder of this paper is organized as follows. Descriptions of the gale background, data used, and model configuration are presented in section 2. Evaluation of the simulation and the flow structure and evolution are provided in sections 3 and 4, respectively. Mountain drags are analyzed in section 5. Following a discussion in section 6, a summary and our conclusions are presented in section 7.

2. WRF Model setup, data, and case description

a. Background and case description

CM is located on the southeastern edge of the Tibetan Plateau (Figs. 1a,b). There are 19 peaks with elevations >3500 m MSL with a base height of ~2000 m MSL. The mountain exhibits a zigzag characteristic due to embedded small-scale topography. Local time is approximately one hour later than Beijing standard time (BST). The distance from Dali station on the lee side (east) of the mountain to the mountain crest and foot is ~9 and ~4 km, respectively. On average (based on 40-yr statistics), 58 gales are reported annually at Dali station with most occurring during late afternoon in winter

(Yang et al. 2013). An observational analysis revealed that Dali station is dominated by an easterly wind between midnight and afternoon, a westerly wind between afternoon and midnight at elevations lower than 600 m AGL (Dong et al. 2016), and the prevailing surface westerly winds during gale periods (Yang et al. 2013). The upper-air jet is generally located over the southern Tibetan Plateau in winter (Yang et al. 2014).

The gale event, which occurred during the late afternoon on 23 January 2015, can be considered a typical case based on the characteristics of the large-scale upper-level and surface winds. The jet axis at 200 hPa was located just above 30°N, a few hundred kilometers from Dali station (Figs. 2a,b). From 0800 to 2000 BST, the shape of the jet changed slightly from anticyclonic curvature to straight westerly (Fig. 2b), and a short geopotential wave trough at 500 hPa developed to the north of Dali station (Fig. 2d). The enhanced meridional pressure gradient at 500 hPa and the straight upper-level jet strengthened the middle- and upper-level westerly winds. The observed 10-m wind at Dali station shows that the wind speed increased from 5 m s^{-1} at 1500 BST to its maximum (>17 m s^{-1}) at 1800 BST (Fig. 4c, below). Figure 5a, described in more detail below, indicates that

TABLE 1. Parameters of the WRF mesoscale simulation (WRF-MESO) and LES (WRF-LES) model configurations.

Model parameters	WRF-MESO	WRF-LES
Domains	Domain 1–3	Domain 4–5
Resolution (km)	9, 3, and 1	0.333 and 0.111
Grid number	361 × 361 for all domains	361 × 361 and 541 × 541
Nests feedback	2-way	2-way
Model top	10 hPa	10 hPa
Vertical levels	86 stretched eta levels	86 stretched eta levels
Depth of the lowest 20 layers (m)	17, 33, 42, 52, 61,70, 77, 83, 88, 93, 97, 103, 106, 112, 117, 122, 126, 132, 136, and 139	17, 33, 42, 52, 61,70, 77, 83, 88, 93, 97, 103, 106, 112, 117, 122, 126, 132, 136, and 139
Upper-atmosphere damping depth (m)	5000.0	5000.0
Time step (s)	18.0, 6.0, and 2.0	0.67 and 0.2
Background and lateral boundary conditions	NCEP-FNL	NCEP-FNL
Land surface	Noah	Noah
Land use	USGS 28 categories	USGS 28 categories
Surface layer	Revised Jimenez	Revised Jimenez
Lake physics	On	On
Erhai Lake temperature	Observed (11.5°C)	Observed (11.5°C)
Planetary boundary layer	Shin–Hong scale-aware	Shin–Hong scale-aware and none
Subgrid-scale turbulence	None	None and TKE 1.5
Cumulus	Kain–Fritsch, none, and none	None
Microphysics	WSM6	WSM6
Radiation	RRTMG	RRTMG

the westerly wind in Dali extends from 1500 m (above ground) to the surface during this period.

b. WRF Model setup and data

The simulations for this study were conducted using the WRF Model, version 3.8.1., which is suitable for a broad range of applications across various scales from LESs to global simulations (Skamarock et al. 2008). In this study, the WRF Model was nested as five domains (D01–D05; Fig. 1a), which were configured for a mesoscale simulation (D01–D03; hereinafter WRF-MESO) and an LES (D04–D05; hereinafter WRF-LES). The outermost domain (D01: 9-km resolution) covered most of the Tibetan Plateau as well as a large area to the east and south. The innermost domain (D05: 111-m resolution) was defined to place CM and Erhai Lake at its center. The atmosphere was discretized vertically as 86 eta levels. The vertical resolution was higher in the lowest few kilometers for optimal determination of the vertical structure of the PBL turbulence and flows. The first model layer was ~17 m deep, and 21 layers (average depth of 90 m) were included within the lowest 2 km AGL (Table 1). The dynamics options of the model were default settings, except for a damping layer imposed in the upper 5 km of the atmosphere to prevent contamination by unphysical wave reflections from the model lid (Klemp and Lilly 1978). The model top was set at 10 hPa. The parameters involved in the two modes of simulation are summarized in Table 1. For all five domains, the physics options included the

rapid radiative transfer model longwave and short-wave radiation scheme (RRTMG; Iacono et al. 2008), WRF single-moment 6-class microphysics scheme (WSM6; Lim and Hong 2010), and Noah land surface model (Ek et al. 2003). The new eta Kain–Fritsch convective scheme (Kain 2004) was active in only the outermost domain. Domains D03 and D04 had horizontal grid spacings of 1 km and 333 m, respectively. These are known as the "gray zone" because only the partial PBL turbulence can be resolved (Wyngaard 2004). To overcome this problem, the Shin–Hong scale-aware PBL scheme (Shin and Hong 2015) was selected for domains D01–D04. For the finest-resolution domain, most PBL turbulence could be resolved. Subgrid-scale turbulence was closed using a turbulent kinetic energy (TKE) 1.5-order closure, and all default parameters were chosen (Talbot et al. 2012). In recognition of the importance of Erhai Lake, located ~5 km east of CM, the lake physics scheme was activated (Gu et al. 2015).

The simulations used NCEP Final Analysis (NCEP-FNL) products as the background initial conditions and the lateral boundary conditions. Observations from more than 2000 surface measurements and 200 soundings from Chinese National Weather stations were also assimilated into the initial fields using the WRF 3D variational data assimilation. All observations provided by the China National Meteorological Center of the China Meteorological Administration were quality checked. Data were also obtained from automatic weather stations (Fig. 1b), which were deployed during

the Sino-Japan Joint Research Center of Meteorological Disaster project involving the Japan International Co-operation Agency (Zhang et al. 2012). One of these stations, located 100 m east of the western shore of Erhai Lake, obtains regular observations of the lake surface temperature. In comparison with the observations from Erhai station, the lake surface temperature of the NCEP-FNL product is overestimated by approximately 13 K. Therefore, for better representation of the lake effect, the temperature for the entire lake surface was corrected during model initialization. This procedure considerably improved the lake surface simulation (not shown). Because the finest geographic dataset in WRF is 30 s, we adopted the 3 s Shuttle Radar Topography Mission (Farr et al. 2007) digital elevation data in domains D04 and D05. To ensure stability in the numerical integration and exclude the spurious grid-point gravity waves, a high-pass filter was applied to the elevation data twice (Beljaars et al. 2004) to exclude scales below 600 and 400 m in domains D04 and D05, respectively.

3. Simulation evaluation

As is known, the evaluation of a numerical simulation has some inherent uncertainties when compared with local observations (von Storch 1995; Jiménez et al. 2010). In addition, small changes in the background flow can yield large changes in the responses in downstream mountain waves (Vergeiner and Lilly 1970; Georgelin and Lott 2001). To include more information about the strong wind spatial variation aroused from the inevitable uncertainties from the topography and upstream atmosphere, we use multiple grid points around the observation in the surface wind simulation evaluation.

a. Surface temperature distribution and wind series

The simulated and observed 2-m temperatures at 1800 BST in WRF-LES D05 and WRF-MESO D02 are shown in Figs. 3a and 3b, respectively. In the WRF-LES D05, the positive upstream–downstream temperature gradient is better simulated than in WRF-MESO D02. Notably, the 2-m temperature gradient along the eastern slope is better simulated in WRF-LES D05 than in WRF-MESO D02. The regional averaged bias and root-mean-square error show comparable magnitudes for WRF-LES D05 and WRF-MESO D02. However, the WRF-LES can capture finer surface temperature distributions related to topography.

The time series of observed and simulated wind variations in the upstream region (denoted as A in Fig. 6d, below) and downslope region (denoted as B in Fig. 6d,
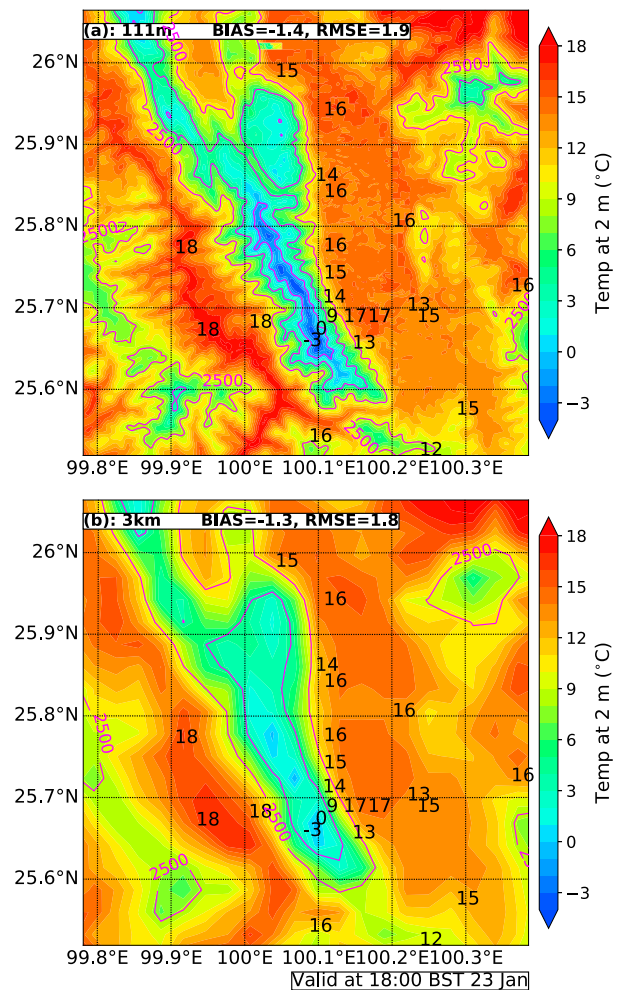

FIG. 3. Simulated (shaded) and observed (numbers) 2-m temperature in (a) WRF-LES D05 (111 m) and (b) WRF-MESO D02 (3 km).

below) are shown in Fig. 4. The observed wind speed increased slightly at A and the wind direction switched from southerly to northerly at midday. The simulated wind at most of the grid points showed similar trends (Figs. 4a,b). At B, the amplitude of the observed and simulated wind speed abruptly increased from less than 7.5 m s^{-1} in the morning (before 1200) to above 10 m s^{-1} (the maximum speed can reach 17 m s^{-1}) in the afternoon. Although the wind direction at B was more complicated, it generally remained westerly in the afternoon and evening (1500–2100 BST). These results show that the WRF-LES could capture the wind evolution trends in both the upstream and the downslope regions, which were discussed in this section.

b. Wind profile evolution

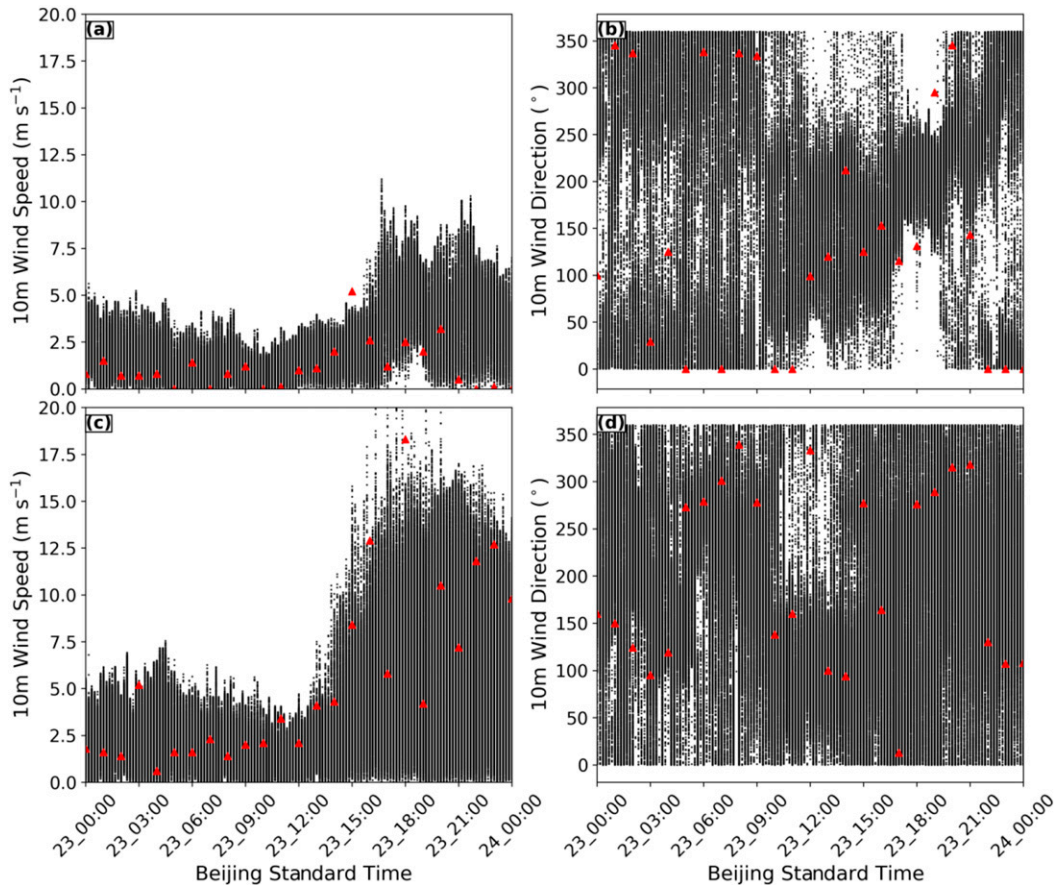The wind profile within the lowest 2 km AGL is operationally observed by an LQ-7 wind profile radar at

FIG. 4. Observed (red triangles) and simulated (black dots) (a),(c) 10-m wind speed (m s^{-1}) and (b),(d) wind direction; the observations were acquired from the (a),(b) upstream (25.68°N, 99.95°E) and (c),(d) downslope (25.7°N, 100.18°E; Dali station) regions (shown by blue squares in Fig. 6d, below). Simulated data that represent the upstream [in (a) and (b)] and downslope [in (c) and (d)] regions are from the red-dash-outlined boxes around the corresponding observation locations denoted as A and B in Fig. 6d, below.

Dali station (located at the same position as the surface observation). The evolution trends of the observed zonal wind u, meridional wind v, and vertical wind w are shown in Figs. 5a, 5d, and 5g, respectively. The evolution of the observed wind profiles can be divided into three stages in terms of the zonal wind speed. The period during which the westerly wind extended to the surface is defined as stage 2 (denoted as S2 in Fig. 5a), and the periods before and after S2 are defined as stage 1 (S1) and stage 3 (S3), respectively.

In stage 1 (before 1500 BST), the wind speed was reasonably small and the wind direction was easterly below 1000 m AGL, while a relatively stronger northwesterly wind dominated the layer above 1000 m AGL. A westerly wind dominated the entire layer below 1500 m AGL during stage 2 (1500–2000 BST). An updraft layer was present in this stage at Dali station, but a period with a relatively weak updraft occurred during 1600–2000 BST (Fig. 5g). In stage 3 (after 2100 BST),

the strong westerly region moves off the ground again, similar to in stage 1.

A grid point from the downslope wind regime (box B; Fig. 6d) is selected for comparison with the observations. The distance (~3 km) between the grid point and the station could be acceptable considering the uncertainties from the large-scale atmosphere forcing, surface properties and topography, and the nonlinear interaction between the downslope wind, rotors, and vortices. The evolution trends of the simulated wind profiles from WRF-LES D05 and WRF-MESO D02 are shown in Figs. 5b, 5e, and 5h and in Figs. 5c, 5f, and 5i, respectively. The period with a weak updraft present in the observed wind profile was captured in the WRF-LES D05 during 1700–2000 BST (Fig. 5h). Conversely, the evolution trends from the WRF-MESO D02 could not successfully capture the wind variation in the three stages detected in the observations. Therefore, the WRF-LES was considered to
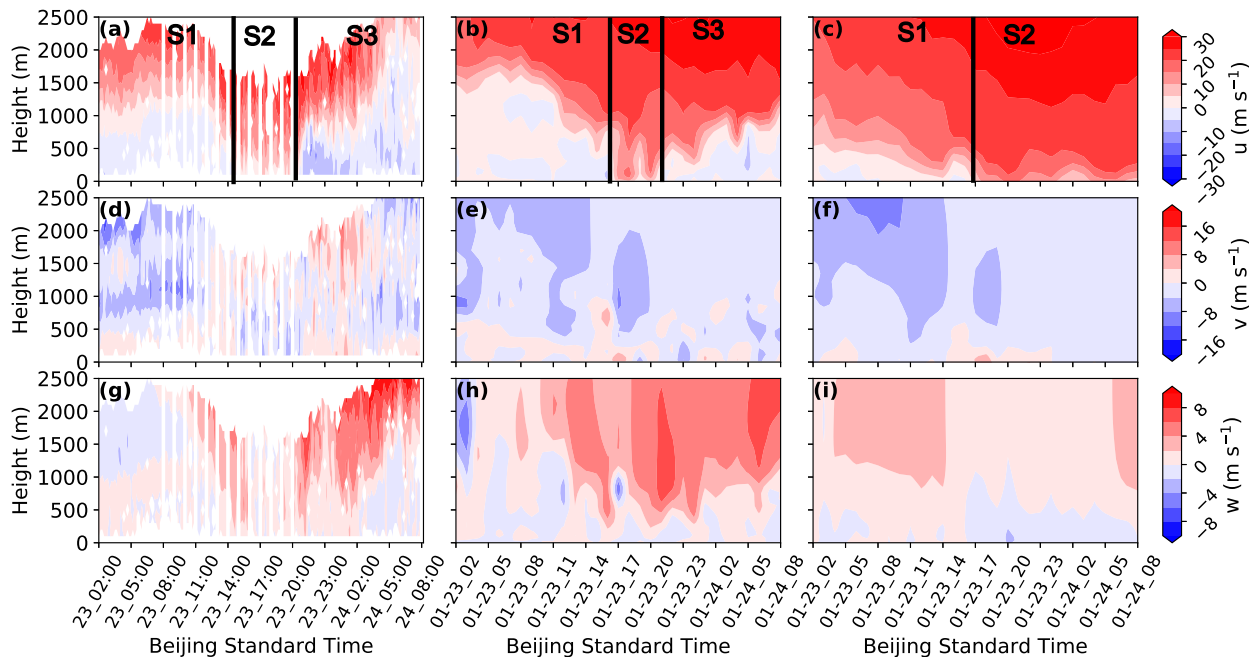
FIG. 5. The (a)–(c) zonal wind, (d)–(f) meridional wind, and (g)–(i) vertical wind from (left) observations and simulations from (center) WRF-LES D05 and (right) WRF-MESO D02. Vertical black lines show the three stages. Vertical coordinates denote height AGL.

be successful in simulating the evolution trends of the wind profile.

Note that the interaction between outer-domain and inner-domain simulations occurs in the two-way simulation. A comparison between one-way and two-way simulations shows that the WRF-LES is better than WRF-MESO in a one-way nested simulation. Furthermore, the WRF-LES in a two-way nested simulation is better than that in a one-way nested simulation for both 2-m temperature distribution and wind profile evolution corresponding to Fig. 3 and 5 (figures not shown).

4. The structure and evolution of flows

In this section, the spatial structure and temporal evolution of the flows are investigated. As indicated in section 3, the studied event presented three stages, where stage 2 was the primary focus of this study. However, stage 1 was also investigated for comparative purposes to highlight the scope of the differences in stage 2.

a. Surface wind

The averaged 10-m wind during 0600–0800 BST and during 1700–1900 BST is shown in Figs. 6a and 6b, respectively. In contrast to stage 1 (Fig. 6a), a strong downslope wind appeared along the eastern slope in the late afternoon (stage 2, shown in Fig. 6b).

Figures 6c and 6d show the region with 10-m wind speeds >12 m s^{-1} during 0600–0800 BST and during

1700–1900 BST. In the morning (Fig. 6c), the 10-m wind speed was relatively small over downstream region. However, three bands of severe wind (>12 m s^{-1}) were evident from west to east in the late afternoon (Fig. 6d). The first was along the crest and eastern slope, the second was separated into two roughly symmetrical northern (approximately 25.9°N, 100.15°E) and southern (approximately 25.65°N, 100.25°E) parts, and the third was in the convergence region (25.6°–25.9°N, 100.3°–100.4°E).

The severe wind was not confined to only the downslope region but was also present in other downstream bands. The wind speed and wind direction in the southern part of the second severe wind region, denoted as C in Fig. 6d, are shown in Fig. 7a and Fig. 7b. The observations confirm that the wind speed did reach the gale criterion (17 m s^{-1}) in this region (Fig. 7a). As in the corresponding observation, the simulated wind displayed an abrupt increase in wind speed in stage 2. The wind evolution in the third severe wind band (convergence region) is presented in Figs. 7c and 7d. In box D (shown in Fig. 6d), the wind speed also experienced an abrupt increase after 1600 BST, and the wind direction remained southerly throughout the simulated day.

b. Evolution of 3D wind structure

1) MACROSTRUCTURE

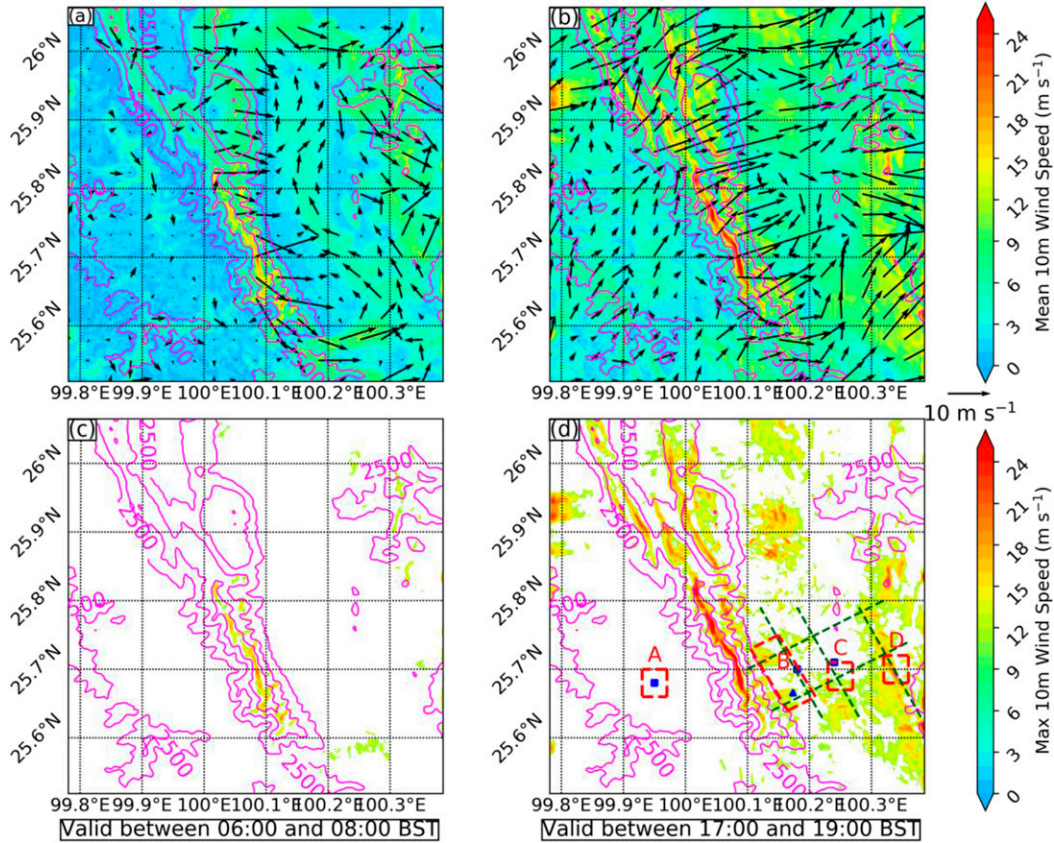The vertical structures of wind speed and potential temperature along 25.7°N, averaged in the early morning

FIG. 6. Averaged 10-m wind vector (arrows) and wind speed (m s^{-1}; shading) during (a) 0600–0800 BST and (b) 1700–1900 BST 23 Jan 2015. (c),(d) Maximum 10-m wind speed in the two corresponding intervals in (a) and (b); wind speed under 12 m s^{-1} is not displayed. Magenta contours show terrain height at 500-m intervals. In (d), blue squares indicate the location of the observations shown in Figs. 4 and 7, red boxes denoted as A–D are regions from which the simulated 10-m wind data were taken for comparison with the observations in Figs. 4 and 7, the blue triangle indicates the location from which the simulated wind profile data were taken for comparison with the wind profile radar observations in Fig. 5, and the two mountain-perpendicular and three mountain-parallel dashed dark-green lines indicate the sections shown in Figs. 9 and 10 (below), respectively.

and late afternoon, are shown in Figs. 8a and 8b, respectively. In stage 1 (early morning), the wind speed increased rapidly from 2 to 10 km MSL in the upstream region. A blocking layer (with negative zonal wind) of approximately 1 km depth was found in both the upstream and downstream lowest levels, and the upper-layer jet (>50 m s^{-1}) was evident above 10 km MSL. This indicates an atmospheric environment with a strong vertical shear. Because of the deep blocking layer, the effective height and width of the mountain decreased (Fig. 8a). In the downstream, weak lee waves were found above 3 km MSL, and the amplitude of which decayed vertically. In stage 2 (late afternoon), the upstream lower-level blocking layer nearly disappeared, increasing the effective mountain height and width. The upper-level jet also increased compared with stage 1, which may have enhanced the vertical shear. In the downstream region, stronger lee

waves were evident above 2.5 km MSL. A reverse flow region was evident beneath the crest of the lee wave, which indicates the possible presence of rotors.

Horizontal sections of time-averaged zonal wind and wind vectors near the crest (at 3200 m MSL) and meridional wind and wind vectors near the foot (at 2200 m MSL) are shown in Figs. 8c–f. At the near-mountain-crest level in stage 1, the wind direction was generally northwesterly over both upstream and downstream regions, and a strong–weak–strong zonal wind pattern was found at the lee of the mountain with a relatively narrow spacing. Conversely, in stage 2, the upstream northwesterly wind shifted to a westerly and the spacing of the strong–weak–strong zonal wind more than doubled. This change corresponds to the change in the lee waves shown in Figs. 8a and 8b.

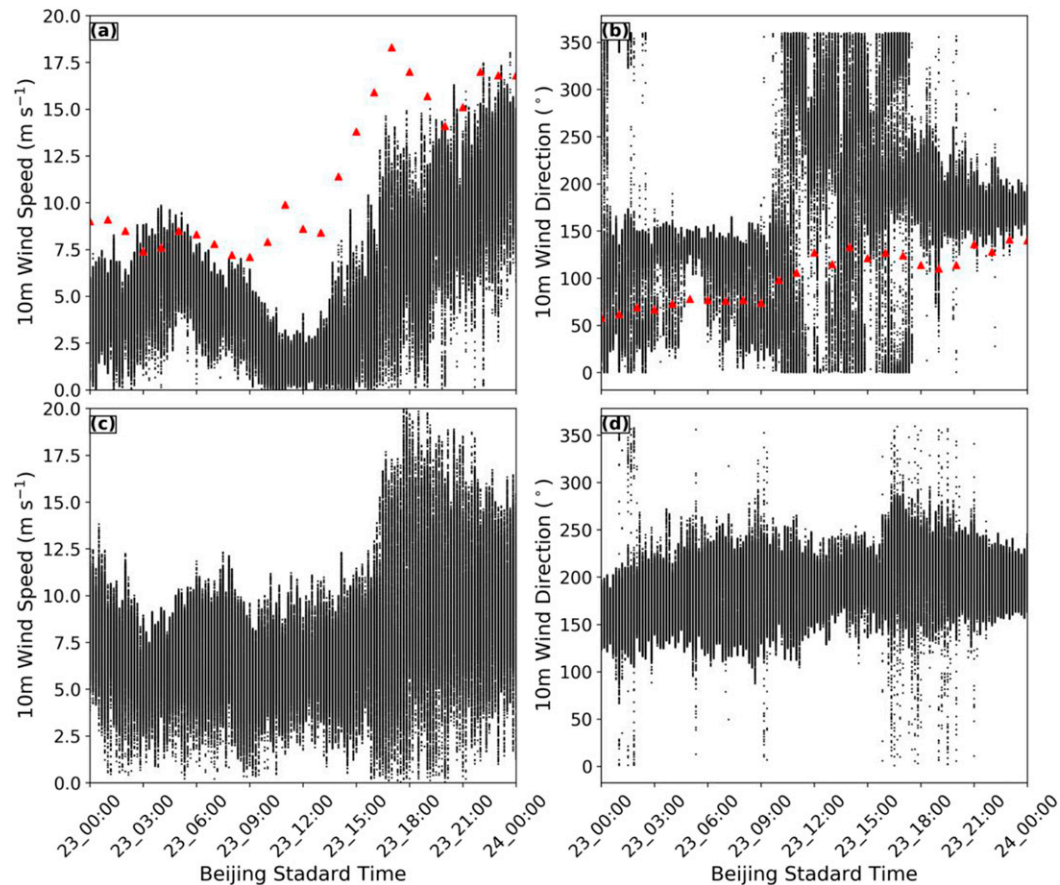At the near-mountain-foot level in stage 1, a north-westerly wind was found in the upstream valley, and

FIG. 7. As in Fig. 4, but for regions C and D; there were no observations in region D.

two horizontal lee vortices were present in the down-stream region (Fig. 8e). In stage 2, the upstream north-westerly wind shifted southwesterly, its speed increased (Fig. 8f), and the two lee vortices also became enhanced (Fig. 8f). Overall, apart from the enhancement of the upper-level jet and slight low-level wind veer, the most significant change is the upstream low-level incident of wind increase and the lee waves and rotors enhancement from early morning to late afternoon.

2) THE INTERACTION AND COHERENT STRUCTURE OF DOWNSTREAM MOUNTAIN FLOWS

To explore the possibility of a severe surface wind prediction in the downstream region, the interaction and coherent structure of the downslope wind, rotors, and vortices are explored. Two perpendicular-mountain sections (positions shown in Fig. 6d) of cross-mountain wind and potential temperature are shown in Figs. 9a and 9b, respectively. The reverse flow was evident in both sections beneath the wave crest, with the northern section located within the lowest layer and the southern

section lifted to 3 km MSL. The downslope wind ex-tended to the foot of the mountain along both sec-tions, but it extended farther downstream along the southern section. The second trough of the lee wave was located just above the eastern 5-km-wide part (110.3°–110.35°E), that is, at the convergence region identified in section 4a.

Two perpendicular-mountain sections of along-ridge vorticity and wind vector are shown in Figs. 9c and 9d. Two 15-km-wide × 3-km-high rotors were found in the two sections with a series of subrotors. The scale, inten-sity, and shape of the rotors and subrotors were broadly similar to the results of a 3D idealized LES (Doyle and Durran 2007). A sheet of high along-ridge vorticity along the lee slopes of the mountain was generated and lifted aloft by the waves where the flow separated.

The coherent structure of the vertical reverse flows and low-level horizontal vortices can influence the spe-cific severe wind distribution. As shown in Figs. 6b and 8f, the northern branch easterly wind of the southern vortex was coincident with the reverse flow along the northern section, whereas the southern branch westerly
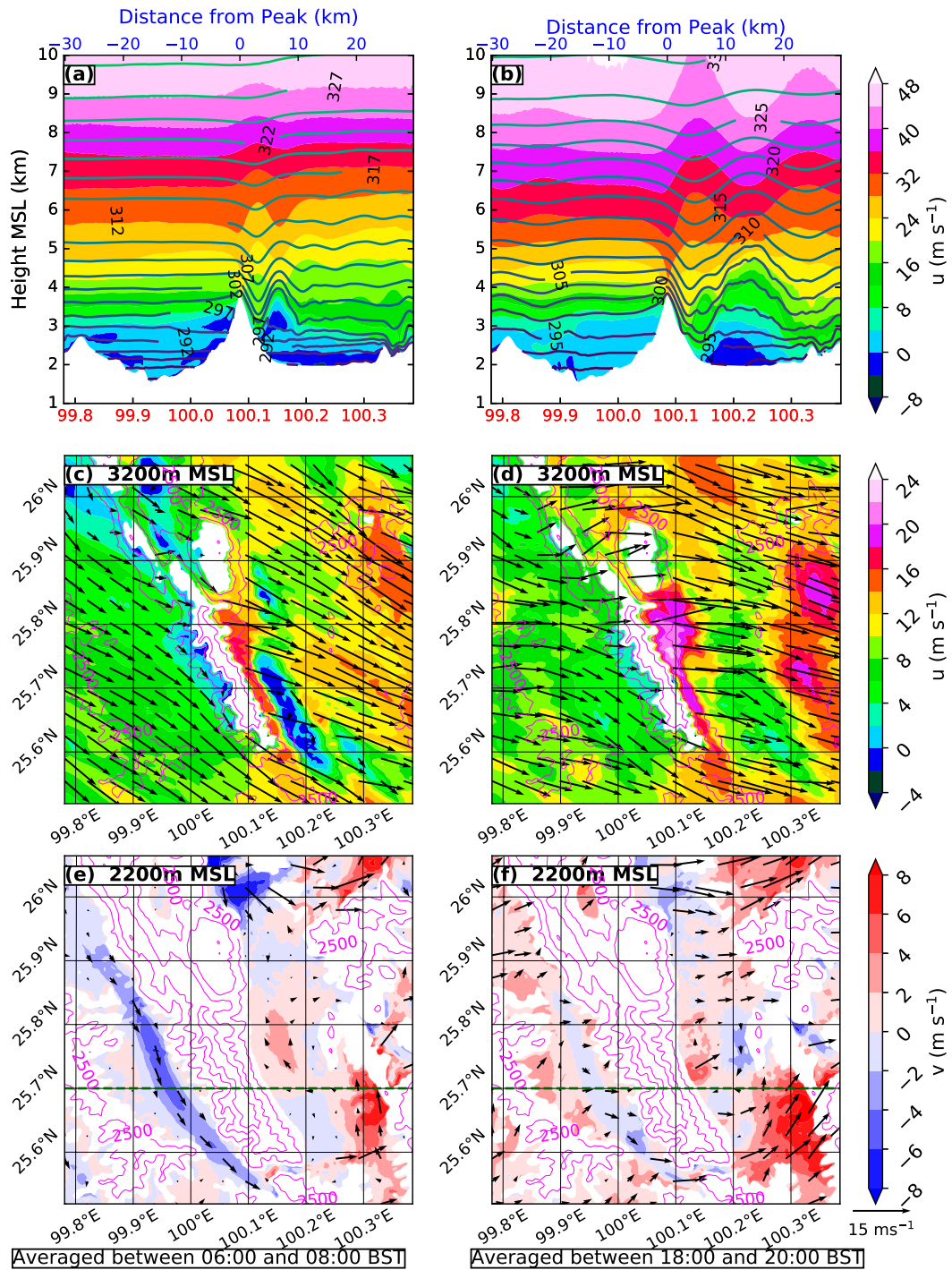
FIG. 8. (a),(b) Vertical section of wind speed (shading) and potential temperature isentropes (contours) and horizontal sections of time-averaged (c),(d) zonal wind (shading) and wind vectors (black arrows) at 3200 m MSL and (e),(f) meridional wind and wind vectors (black arrows) at 2200 m MSL, averaged during (left) 0600–0800 and (right) 1800–2000 BST 23 Jan 2015. The dashed dark-green line in (e) and (f) indicates the position of the vertical cross section shown in (a) and (b).
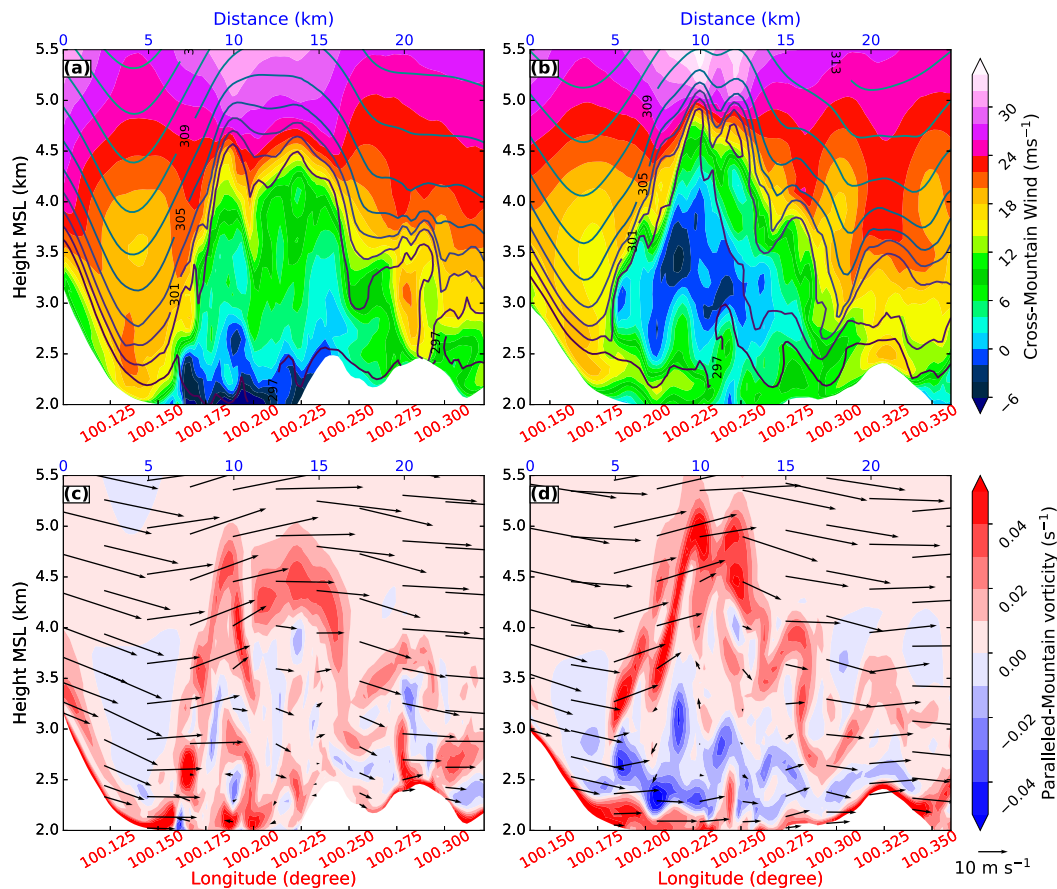
FIG. 9. Vertical section of cross-mountain wind speed (shading) and potential temperature isentropes (contours) along (a) northern and (b) southern perpendicular-mountain lines (the two mountain-perpendicular dashed dark green lines in Fig. 6d) at 1810 BST 23 Jan 2015. (c),(d) As in (a) and (b), but for the along-ridge vorticity and cross-mountain-vertical wind vector.

wind of the southern vortex was coincident with the low-level westerly wind along the southern section. This affected the extent of the downslope wind, which was identified as extending farther downstream along the southern section.

Three along-ridge sections of cross-mountain wind are shown in Fig. 10 as wind vectors in these sections. A comparison of the western and middle sections revealed that the downslope wind and reverse wind have a close relationship. For example, the downslope wind shown in southern part of the western along-ridge section (25.66°N) can extend farther east because the reverse wind was lifted above it (1.0–2.0 km AGL). The downslope wind at 25.7°N (in Fig. 10a) cannot extend much because the reverse wind was strong there. The vortex can also influence the downslope wind and reverse wind. In the middle along-ridge section, the reverse wind was lifted in the southern section by a southwesterly low-level flow (25.63°–25.71°N, 0–1 km). Comparing this flow with the corresponding region in

Fig. 8f, the southwesterly wind was identified as the southeast branch of the southern vortex in Fig. 8f, which is tangent to the downslope flow but opposite to the reverse flow. The rotor reverse flow and vortex reverse flow were combined together from 25.72° to 25.8°N, which strengthened the reverse flow and prevented the downslope wind. The eastern along-ridge section shows a thin convergence layer (0–0.5 km in Fig. 10c), where a strong cross-mountain wind ($>18\,\mathrm{m\,s^{-1}}$) was found. This region was identified as the third region of severe wind (Fig. 6d) and the trough of the lee wave (Fig. 8b). The three branches of the flow converged here, which induced severe wind.

The detailed orography also influenced the wind pattern. As displayed in Fig. 10a, the downslope wind was found to be related to the height of the mountain. The downslope wind extends farther in the downstream region of the low ridge area. The coefficient of correlation between the mountain height and the cross-mountain wind at the first level in the western
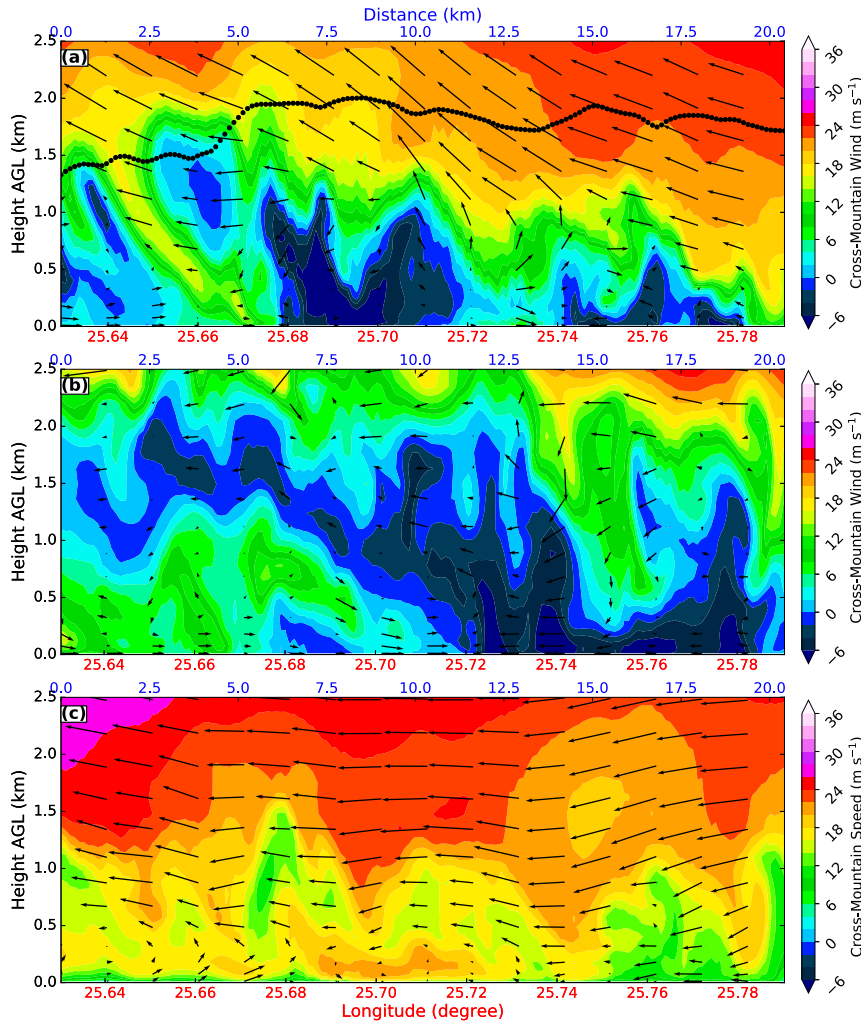
FIG. 10. Vertical section of cross-mountain wind speed (shading) and along-ridge vertical wind vector along the (a) western (downslope), (b) middle (rotor), and (c) eastern (convergence) along-ridge lines (the three mountain-parallel dashed dark-green lines in Fig. 6d) at 1810 BST 23 Jan 2015. The black dotted line in (a) shows the difference between the mountain height and terrain height along the western along-ridge line.

along-ridge section was −0.44. This indicates that the extent of the downslope wind was related to the upstream mountain height.

In summary, the downslope wind, vertically rotated rotors, and horizontally rotated vortices are highly interrelated. The surface severe wind is the result of the combined impacts of the different flow systems, which is further related to the upper mountain waves and topography.

c. Mechanism of lee-wave evolution

One remaining unsolved question is why the lee waves became lengthened and amplified in the afternoon. Generally, there are two groups of theories to explain downslope wind events. One group focuses

more on the linear trapped lee waves and accounts for the downslope windstorm to the resonant waves (Scorer 1949; Scorer and Klieforth 1959; Clark and Peltier 1984), while the other group stresses the nonlinear wave breaking as the severe wind mechanism on the downslope (Long 1953, 1955; Clark and Peltier 1977; Clark and Farley 1984). The latter one suggests a stationary turbulent layer with strong mixing over the mountain, which is not found in the present case. Unlike the waves caused by substantial topography with long horizontal wavelengths (Brinkmann 1974; Jiang and Doyle 2004), the trapped lee waves are more likely triggered by small-scale mountains (Scorer 1949; Corby and Wallington 1956; Aanensen 1965; Pearce and White 1967), which are similar to the present wave pattern shown in Fig. 8.

Moreover, the trapped linear-wave theory requires a rapid increase in wind speed and/or a decrease in flow stability with height, which also resembles the presented case.

The simulated upstream profiles at 0700 and 1800 BST 23 January 2015 are presented in Fig. 11. The quantities were averaged in a 4 km × 4 km box 25 km upstream from the mountain. A strong wind shear layer existed in the troposphere, where the wind increased rapidly with altitude to its maximum at approximately 10 km MSL in both the early morning and late afternoon. A quasi-two-layer troposphere comprising a less stable layer (5–10 km) situated above a strong stable layer (2.5–5 km) was present in the early morning. A three-layer-structure troposphere was shown in the late afternoon with a much smaller Scorer parameter layer under 3.8 km MSL, an elevated strong stable layer at 4 km MSL and less a stable layer above 4.5 km MSL. Because the Scorer parameter decreased immediately above the top of the mountain in both early morning and late afternoon, short gravity waves induced by the mountain could not propagate upward through the troposphere. Therefore, these waves remained trapped as lee waves within the lower troposphere.

In the morning, a deep blocking layer was shown that was due to the high nondimensional mountain height (Fig. 15, described in more detail below) from high stability. The deep blocking layer made the effective size of the mountain very small. As a result, only small lee waves were showed in the morning. In the afternoon, the low-level wind increased considerably, which induced the disappearance of the blocking layer and a large effective size of the mountain. The increased upstream wind can contribute to lengthening of the lee waves. The vertically straight profile of potential temperature in the low-level troposphere indicated that a neutral or weakly convective PBL existed in the late afternoon. The deepened mixing of PBL elevated and thinned the very stable layer just above it, which was suggested to be the main cause of the systematic temporal increase in the horizontal wavelength (Ralph and Neiman 1997). Three-layer theoretical studies also showed that lee waves are lengthened when the upstream low-level wind is increased and a neutral PBL is present under an inversion layer (Pearce and White 1967; Wang et al. 2010). Observations have also shown that the wavelengths of lee waves generally increase during the daytime, in response to surface heating, and decrease after sunset (Gerbier and Berenger 1961; Mitchell et al. 1990; Ralph and Neiman 1997). These statements are consistent with the Dali gales as derived from long-term observations (Yang et al. 2013). More recently, using a linear theory, Lott (2016) showed that the null surface wind and wind

shear in the lower troposphere can induce very large-amplitude lee waves without wave breaking above. A similar situation is clearly shown in Fig. 11. In the present case, the upper-layer jet was enhanced in the afternoon (Figs. 8a,b), which may increase the wind shear in the troposphere. However, other simulations suggested that the linear theory can reasonably predict the wavelength but largely underestimate the wave amplitude (Vosper 2004; Hills et al. 2016; Sachsperger et al. 2017). The uncertainties in the nonlinear processes are discussed in section 6. Overall, with the large-scale upper-level jet and local upstream wind persistence or enhancement, the increased low-level incident flow and wind shear in the troposphere, deepened mixing PBL, and large effective mountain size may be combined and contribute to the lengthening of the lee waves.

5. Topographic drag on the atmosphere

The overall dynamic effect of orography on the atmosphere in mesoscale and large-scale models is accounted for as orographic drags, which are usually parameterized as low-level flow blocking and upper-layer gravity wave breaking (i.e., Lott and Miller 1997) and turbulent orographic form drag (Beljaars et al. 2004). However, the orographic drag triggered by trapped lee waves has not been parameterized for most operational NWP models.

Figure 12 shows the total surface drag induced from the CM in the concerned period for different resolutions. A method that can remove the mean slope from the drag calculation is used to calculate the surface pressure drag (Carissimo et al. 1988; Smith et al. 2006). The surface pressure drags in D05 (111-m grid spacing), D02 (3-km grid spacing), and D01 (9-km grid spacing) all increased from the early morning to the late afternoon. Although the drag direction in different resolution simulations is nearly the same, the drag magnitude can be largely different. In stage 1, the 3-km simulation and 9-km simulation both underestimated the drag with a similar factor of one-half. In stage 2, the drag in the 111-m simulation can be 4 times that in the 9-km simulation. The 3-km simulation underestimates the total drag of approximately $1 \, \text{N} \, \text{m}^{-2}$ in all of the concerned periods. This means that the 3- and 9-km mesoscale simulations missed a large part and most of the total surface drags, respectively. Noted that a two-way nest simulation may mix the ability of resolution and interaction between coarse-grid domains and fine-grid domains. A comparison between one-way nest and two-way nest simulations on the resolved surface drag corresponding Fig. 12 has been done (not shown). The drag direction in both one-way and two-way simulations is closed. The 9-km-resolution simulation
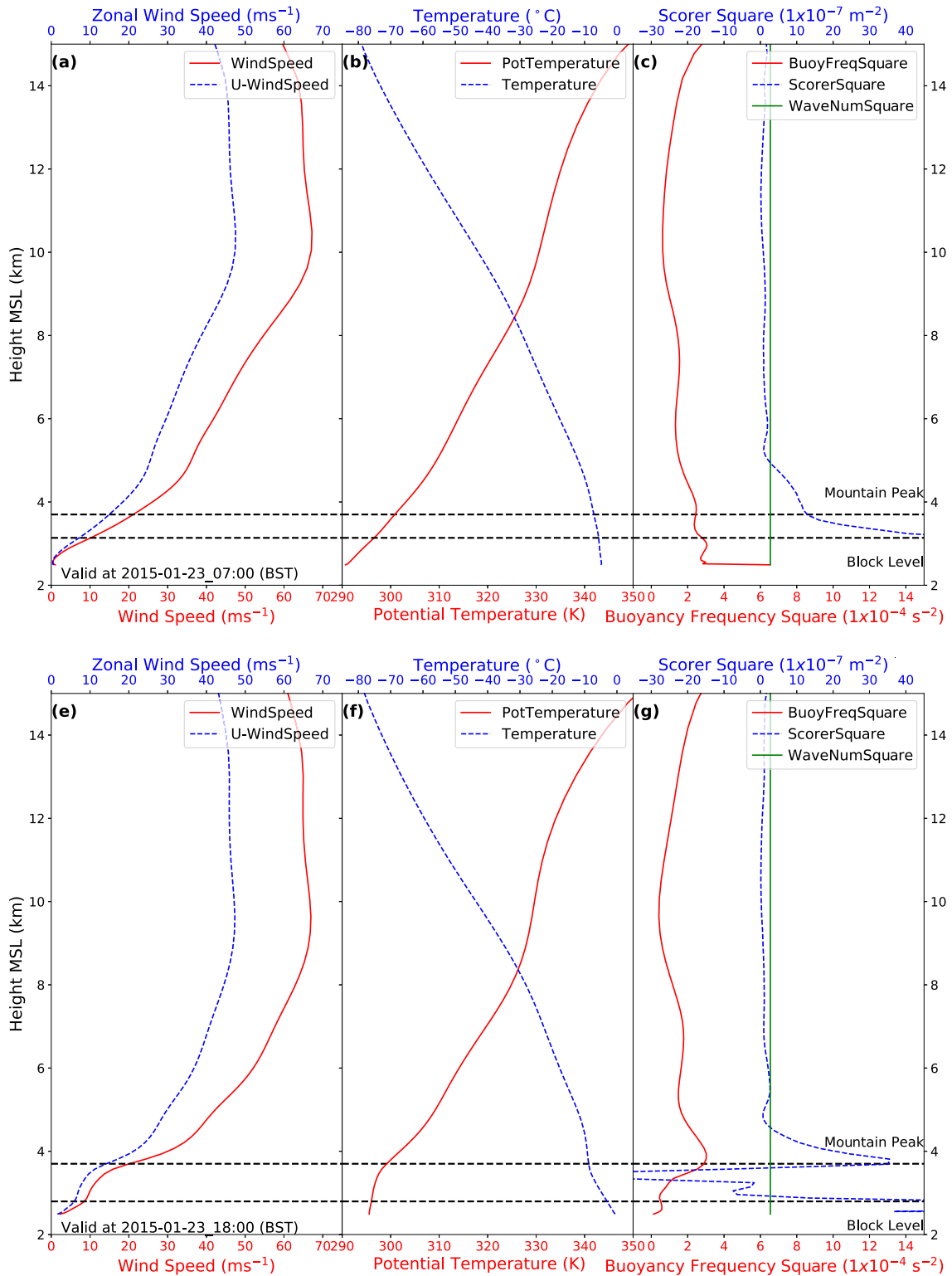
FIG. 11. Simulated upstream profiles of (a),(d) westerly wind speed (m s^{-1}; blue dashed line) and full horizontal speed (m s^{-1}; red solid line), (b),(e) temperature (°C; blue dashed line) and potential temperature (K; red solid line), and (c),(f) the Scorer parameter (10^{-7} m^{-2}; blue dashed line) and buoyancy frequency square (10^{-4} s^{-2}; red solid line) at (top) 0700 and (bottom) 1800 BST 23 Jan 2015. The green lines in (c) and (f) represent the wavenumber square (10^{-7} m^{-2}) of the mountain. Quantities were averaged in a 4 km × 4 km box at 25.7°N, 99.83°N (approximately 25 km upstream from the mountain summit).
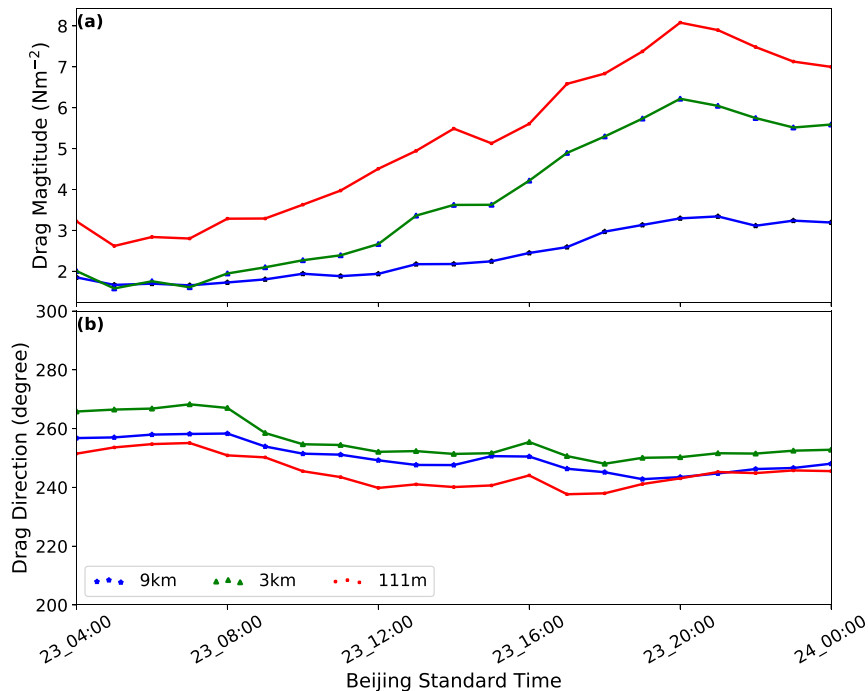
FIG. 12. Resolved surface pressure drag (a) magnitude and (b) direction from 25.5° to 26.0°N and from 99.8° to 100.3°E calculated from D05 (111-m grid spacing; red), D02 (3-km grid spacing; green), and D01 (9-km grid spacing; blue).

can resolve much less (about one-half of) surface drag in a one-way simulation than in a two-way simulation, which may be due to the absence of the feedback from inner domains as the inner domain simulations can resolve more drag than outer domains. The WRF-LES in a one-way simulation can resolve less (about $-0.5\,\mathrm{N\,m^{-2}}$) and comparable surface drag in the morning and afternoon, respectively, than that in a two-way simulation. On the other hand, the 3-km-resolution simulation in a one-way simulation can resolve more (about $0.5\,\mathrm{N\,m^{-2}}$) and comparable surface drag in the morning and afternoon, respectively, than that in a two-way simulation. Overall, both one-way and two-way nest simulations show that the 9-km-resolution simulation can hardly resolve the surface drag in the day concerned, whereas the 3-km-resolution simulation can resolve a part of drag especially in afternoon.

Figure 13 shows the wave-induced vertical flux of zonal momentum and wave-induced stress to the zonal wind at 0700 and 1810 BST. The negative vertical flux of zonal momentum is evident above the downslope wind, which is increased and extended over 10 km MSL in the late afternoon (Figs. 13a,b). This means that zonal momentum is transported downward from where the upper-level jet is located. The positive wave-induced stress along the lee slope that extended downstream favored the acceleration of the horizontal zonal wind

near the surface. The negative wave-induced stress above the severe downslope wind weakened the upper-level zonal wind (Figs. 13c,d). As shown in Fig. 8b, the upper-level wind is clearly decreased over the mountain region compared with the upstream incoming region. The vertical extension of the wave stress can be more than 10 km MSL in the late afternoon, and its magnitude is much larger than that in the earlier morning. Because the waves presented here cannot be fully resolved in mesoscale and large-scale models (i.e., grid spacing is 3 or 9 km), the drag and its impact on the upper-layer jet are also partly or largely missed.

6. Discussion

a. Uncertainties in the simulation

Notably, artificial perturbation (Muñoz-Esparza et al. 2014, 2017; Sauer et al. 2016) are important to developing turbulence in the inflow boundaries of an LES domain for a downstream simulation. However, no perturbation scheme has been applied at the D04 and D05, so turbulence production is necessary to be examined. Figure 14 shows the perturbation vertical velocity in the southeast inflow region of D05 at half PBL height at 1400 BST January 2015. Nearly horizontally homogeneous coherent rolls persist at 20 km × 20 km, and the fetches are not shown here. Meridional
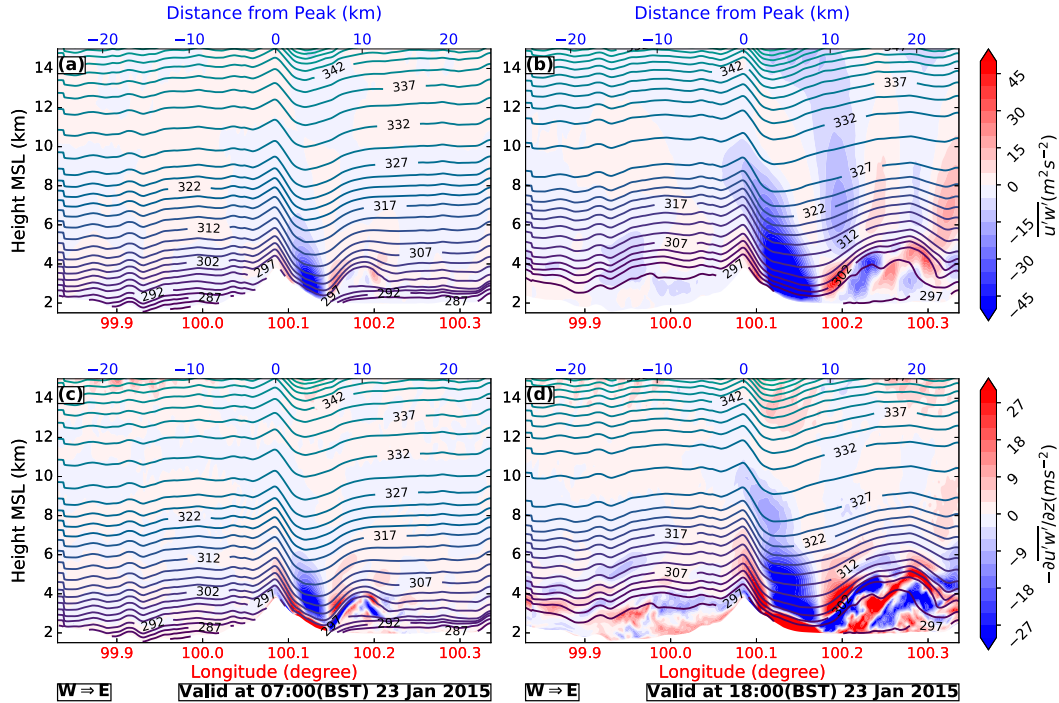
FIG. 13. Wave-induced (a),(b) vertical flux of zonal momentum and (c),(d) forcing to the zonal wind at (left) 0700 and (right) 1810 BST 23 Jan 2015. The section was taken at 25.7°N along the line shown in Fig. 8.

direction evolution of the energy spectra of the perturbation vertical velocity is presented in Fig. 14b for the corresponding region in Fig. 14a. The spectra lines show a production region (TKE $\propto k^{-1}$; $4 \times 10^{-4} < k < 8 \times 10^{-4}$) and an inertial range with a $-5/3$ slope ($8 \times 10^{-4} < k < 2 \times 10^{-3}$). No significant differences are found that are due to different distances to the west inflow edge, which means that the turbulence is well developed in the whole domain during the daytime. During the night, the horizontal distribution of the perturbation vertical velocity shows a similar structure as that in the daytime (not shown). The energy spectra of the perturbation vertical velocity do not display significant differences due to different distances to the west inflow edge as well. As the horizontal grid size is ~100 m, the large eddies in the stable boundary layer can hardly be explicitly resolved at night. Muñoz-Esparza et al. (2017) showed that the WRF nested configured LES could successfully capture global intermittency in night with a horizontal grid size of 8 m. For this case, it is too expensive to adopt such a high resolution to cover a 100 km × 100 km domain and a 36-h simulation. However, van Stratum and Stevens (2015) showed that the consequence of misrepresenting nighttime ABL turbulence on daytime convection is small. In addition, Crosman and Horel (2017) showed that WRF-LES can reproduce a

more realistic overall depth and vertical temperature gradient of the cold-air pool under stable PBL conditions. By using WRF-LES to accurately simulate thermal-driven slope-valley wind under stable conditions during the Terrain-Induced Rotor Experiment in California's Owens Valley, Zhou and Chow (2013) proved the feasibility and usefulness of the nested LES of SBL flows over complex terrain. Although most observations are from surface stations, a wind profile has also been provided (Fig. 5). The observation shows a clear extension of the westerly wind to the surface during the afternoon, which is also shown in WRF-LES and consistent with the amplification wave period. On the other hand, since the surface observations are closely related to the aloft atmosphere evolution and the mountain flow can induce large difference over a short distance (indicated in section 4), the verified surface temperature distribution and surface wind evolution could not be coincident. In addition, the present simulation results match well with the historical large-scale flow pattern and long-term gale observation statistics. Therefore, despite the deficiency in the direct observations of the waves and rotors, the simulation could be credible.

b. Uncertainties of the mechanism

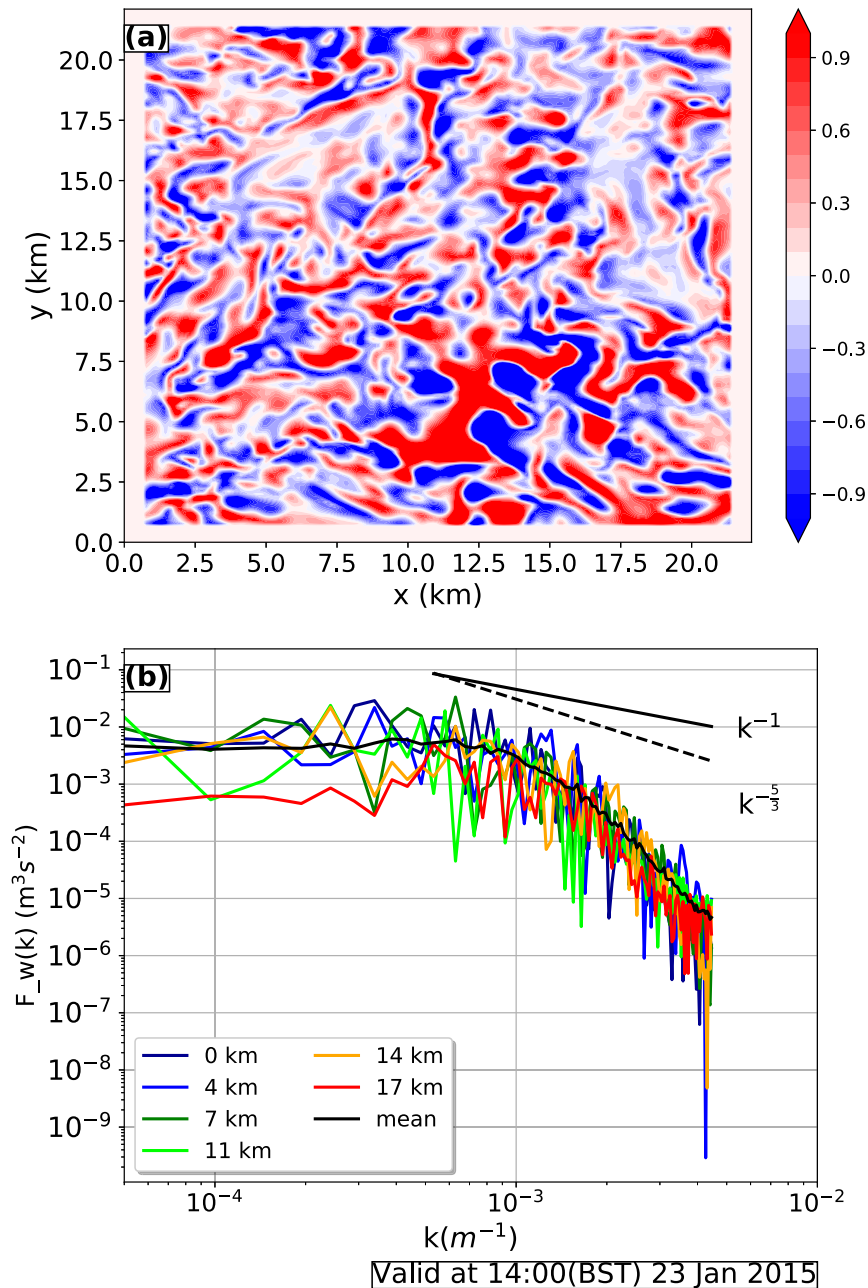It is still challenging to fully convince the mechanism of the wave amplification and lengthening in the present

FIG. 14. (a) Perturbation vertical velocity (m s^{-1}) on a horizontal plane at half PBL height southeast of the D05 at 1400 BST 23 Jan 2015. The blank regions on the four boundaries result from the calculation of the perturbation velocity because the average is taken for the 1.5 km × 1.5 km box. (b) Energy spectra of the perturbation vertical velocity along the y direction at several locations from $x = 0$, 4, 7, 11, 14, and 17 km and x-direction mean corresponding to the domain shown in (a).

realistic simulation, though it can be explained by the lengthened and amplified trapped lee waves. The existing theories that accounted for the trapped lee waves are mostly linear (Scorer 1949; Corby and Wallington 1956; Pearce and White 1967; Zang et al. 2007; Zang and Zhang 2008; Lott 2016), but the nonlinear processes are

clearly involved in the wave evolution. The blocking flows and rotors are shown in the early morning and late afternoon, respectively, and are apparent nonlinear processes. The height and steepness of the mountain are too significant to be considered in a linear regime. On the other hand, most nonlinear theoretical works focus on
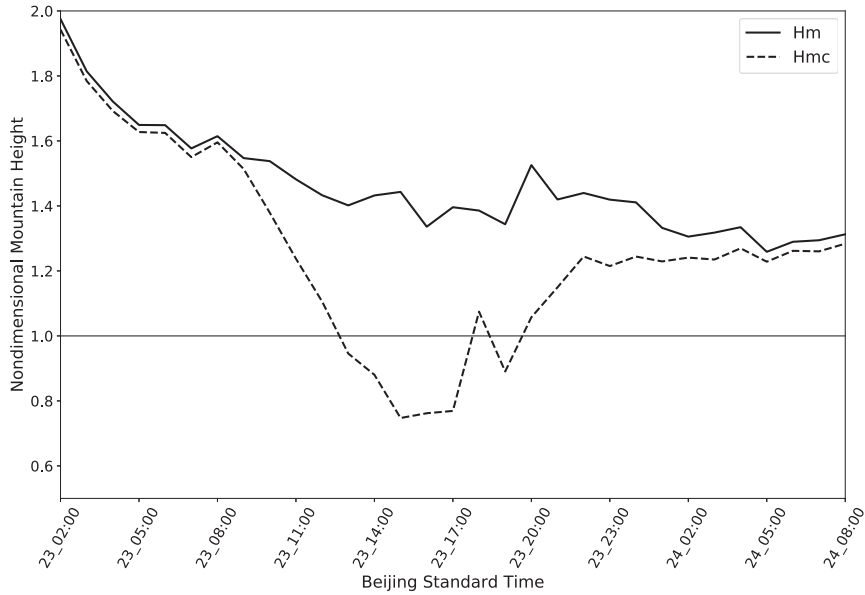
FIG. 15. Nondimensional mountain height evolution. Here, Hm was calculated on the basis of the average value of the zonal wind and the buoyancy frequency at the mountaintop level.

the wave breaking phenomenon (Clark and Peltier 1977; Clark and Farley 1984; Durran 1990) rather than trapped lee waves. However, some numerical simulations have shown that the wavelengths are well predicted by the linear theory but that the wave amplitude is seriously underestimated by the linear theory (Vosper 2004; Hills et al. 2016). From the two-layer and three-layer linear theories, the wavelength is determined by the upstream flow Sorer parameter, wind, and the depth of each layer (Scorer 1949; Corby and Wallington 1956; Pearce and White 1967; Zang et al. 2007; Zang and Zhang 2008). The troposphere displayed a two-layer structure in the early morning (Figs. 11a–c) and a three-layer structure in the late afternoon (Figs. 11d–f). In the early morning, the blocking layer was clearly shown upstream and downstream (Figs. 8a,b). The interaction between the blocking atmosphere and the aloft lee wave is not clear and must be further investigated. During the daytime, as the blocking layer was driven by diabatic surface heating (Kirshbaum 2017), the low-level wind was increased, and the mixing layer was extended higher. The deepened mixing layer and increased upstream wind can both be attributed to the lengthened lee waves (Ralph and Neiman 1997; Udina et al. 2017). In addition, the wind shear in the troposphere can also produce large-amplitude trapped lee waves (Lott 2016). However, these influences from the lower- and upper-layer atmosphere are difficult to determine separately in this realistic simulation.

Sauer et al. (2016) showed that increasing the compensated nondimensional mountain height from 0.55 to 1.0 gradually amplified the trapped lee wave to be transited into nonlinear breaking. Here the wave amplitude is closely related to nondimensional mountain height (Hm = Nh_m/U, where N is the buoyancy frequency, h_m is the mountain height, and U is the incident wind speed) or compensated nondimensional mountain height [Hmc = $N(h_m - z_i)/U_g$; here U_g is defined as the geostrophic wind aligned in the x direction]. The evolution of Hm and Hmc calculated on the basis of the average value of the zonal wind and buoyancy frequency at the mountaintop level is shown in Fig. 15. The Hmc (between 0.7 and 1.0) indicated a large-amplitude lee-wave regime in the late afternoon and upstream blocking in the morning, but wave breaking was not found at 1200 and 2000 BST when the Hmc was approximately 1.0. However, the calculation uncertainties of Hm and Hmc should be noticed because N and U (or U_g) are vertically varied in the realistic simulation but usually uniform or partly uniform in idealized simulations (Reinecke and Durran 2008). Overall, uncertainties exist in understanding the mechanism of lee-wave evolution as a result of low-level blocking and surface heating.

7. Summary and conclusions

A downslope gale event that occurred during the late afternoon on 23 January 2015 was investigated using a realistic-case WRF-based LES to elucidate the dynamical mountain processes related to the gale. The simulation was verified by the regional 2-m temperature

distribution and wind evolution. Verification showed that the simulation is capable of successfully capturing the spatial distribution and the main trends of the wind evolution. The main findings of the study are as follows:

1) A transition from the upstream blocking stage in the early morning to the lengthened and amplified trapped lee-wave stage in the late afternoon has been displayed under the favorable large-scale upper jet and local upstream wind direction on the Tibetan Plateau. Because the large-scale jet is common over this region and the gales are frequently observed in the afternoons during winter at Dali station (Yang et al. 2013, 2014), the stage transition between upstream blocking and large lee waves may also be common in similar situations.

2) The nonlinear interaction between the downslope wind, reverse flow of the rotors and vortices, and the local topography has been investigated and shows that the severe surface wind is closely related to the coherent structure of the involved local wind systems. These wind systems nonlinearly interact with each other and are influenced by topography and mountain waves. The uncertainties associated with the upstream inflow and its turbulence, the surface properties, and topography cannot be completely avoided, which may result in difficulties in severe wind predictions in downstream areas despite high-resolution simulation.

3) The drag analysis indicates that the mesoscale and large-scale (with 3–9 km grid spacing in this study) model may partly or largely miss the mountain drag associated with the upstream blocking and amplified trapped lee waves, which is comparable to the large-scale mountain drag over the Alps (Smith et al. 2006). However, most models have not implemented a trapped lee-wave parameterization in large-scale modeling, and it is recommended to turn off mountain blocking parameterizations in relatively high-resolution (10 km in the WRF user guide) models, as this may induce errors over mountainous regions, such as over and around the Tibetan Plateau.

In addition to the above findings, some unsolved scientific questions are raised, which are mainly associated with the evolution of the upstream blocking and surface heating. The interaction between the low-level blocking in the upstream and downstream regions and the aloft trapped lee waves should be investigated in the future. Although the relationship between blocking and surface heating has been investigated (Kirshbaum 2017) under large-scale conditions, how the blocking layer evolves under a strong westerly jet due to surface heating

remains unclear. The relative importance of the deepened mixing PBL and increased incident upstream low-level wind due to surface heating on the large lee wave should also be investigated, though they can independently contribute to the wave lengthening. The results of this study showed the value of adopting a WRF-LES to investigate mountain-induced wind phenomena, especially the microscale interaction of the flows of the rotors and vortices. The advantages of the WRF-LES were confirmed by verification and microflow structural analysis. Although some uncertainties exist in the simulation that are due to the surface properties and topography, these uncertainties may influence the specific wind distribution, as shown in section 4, but do not hamper the ability to obtain the above conclusions.

REFERENCES

Aanensen, C. J. M., 1965: Gales in Yorkshire in February 1962. *Geophys. Mem.*, **14**, 1–44.

Baklanov, A., and Coauthors, 2011: The nature, theory, and modeling of atmospheric planetary boundary layers. *Bull. Amer. Meteor. Soc.*, **92**, 123–128, https://doi.org/10.1175/2010BAMS2797.1.

Beljaars, A. C. M., A. R. Brown, and N. Wood, 2004: A new parametrization of turbulent orographic form drag. *Quart. J. Roy. Meteor. Soc.*, **130**, 1327–1347, https://doi.org/10.1256/qj.03.73.

Boos, W. R., and Z. Kuang, 2010: Dominant control of the South Asian monsoon by orographic insulation versus plateau heating. *Nature*, **463**, 218–222, https://doi.org/10.1038/nature08707.

Brinkmann, W A E., 1974: Strong downslope winds at Boulder, Colorado. *Mon. Wea. Rev.*, **102**, 592–602, https://doi.org/10.1175/1520-0493(1974)102<0592:SDWABC>2.0.CO;2.

Carissimo, B. C., R. T. Pierrehumbert, and H. L. Pham, 1988: An estimate of mountain drag during ALPEX for comparison with numerical models. *J. Atmos. Sci.*, **45**, 1949–1960, https://doi.org/10.1175/1520-0469(1988)045<1949:AEOMDD>2.0.CO;2.

Chow, F. K., M. Xue, and J. H. Ferziger, 2005: Explicit filtering and reconstruction turbulence modeling for large-eddy simulation of neutral boundary layer flow. *J. Atmos. Sci.*, **62**, 2058–2077, https://doi.org/10.1175/JAS3456.1.

——, A. P. Weigel, R. L. Street, M. W. Rotach, and M. Xue, 2006: High-resolution large-eddy simulations of flow in a steep Alpine valley. Part I: Methodology, verification, and sensitivity experiments. *J. Appl. Meteor. Climatol.*, **45**, 63–86, https://doi.org/10.1175/JAM2322.1.

Clark, T. L., and W. R. Peltier, 1977: On the evolution and stability of finite amplitude mountain waves. *J. Atmos. Sci.*, **34**, 1715–1730, https://doi.org/10.1175/1520-0469(1977)034<1715:OTEASO>2.0.CO;2.

——, and R. D. Farley, 1984: Severe downslope windstorm calculations in two and three spatial dimensions using anelastic interactive grid nesting: A possible mechanism for gustiness. *J. Atmos. Sci.*, **41**, 329–350, https://doi.org/10.1175/1520-0469(1984)041<0329:SDWCIT>2.0.CO;2.

——, and W. R. Peltier, 1984: Critical level reflection and the resonant growth of nonlinear mountain waves. *J. Atmos. Sci.*, **41**, 3122–3134, https://doi.org/10.1175/1520-0469(1984)041<3122:CLRATR>2.0.CO;2.

Corby, G. A., and C. E. Wallington, 1956: Airflow over mountains: The lee-wave amplitude. *Quart. J. Roy. Meteor. Soc.*, **82**, 266–274, https://doi.org/10.1002/qj.49708235303.

Crosman, E. T., and J. D. Horel, 2017: Large-eddy simulations of a Salt Lake Valley cold-air pool. *Atmos. Res.*, **193**, 10–25, https://doi.org/10.1016/j.atmosres.2017.04.010.

Decker, S. G., and D. A. Robinson, 2011: Unexpected high winds in northern New Jersey: A downslope windstorm in modest topography. *Wea. Forecasting*, **26**, 902–921, https://doi.org/10.1175/WAF-D-10-05052.1.

Dong, B., J. Li, J. Sun, A. Xu, and J. Su, 2016: Vertical structure and variation characteristics of wind field in low-level atmosphere in the southeastern margin of Qinghai-Xizang Plateau. *Plateau Meteor.*, **35**, 597–607.

Doyle, J. D., and D. R. Durran, 2007: Rotor and subrotor dynamics in the lee of three-dimensional terrain. *J. Atmos. Sci.*, **64**, 4202–4221, https://doi.org/10.1175/2007JAS2352.1.

Durran, D. R., 1986: Another look at downslope windstorms. Part I: The development of analogs to supercritical flow in an infinitely deep, continuously stratified fluid. *J. Atmos. Sci.*, **43**, 2527–2543, https://doi.org/10.1175/1520-0469(1986)043<2527:ALADWP>2.0.CO;2.

——, 1990: Mountain waves and downslope winds. *Atmospheric Processes over Complex Terrain, Meteor. Monogr.*, No. 45, Amer. Meteor. Soc., 59–81.

Ek, M. B., K. E. Mitchell, Y. Lin, E. Rogers, P. Grummann, V. Koren, G. Gayno, and J. D. Tarpley, 2003: Implementation of Noah land surface model advances in the NCEP operational mesoscale Eta model. *J. Geophys. Res.*, **108**, 8851, https://doi.org/10.1029/2002JD003296.

Farr, T., and Coauthors, 2007: The Shuttle Radar Topography Mission. *Rev. Geophys.*, **45**, RG2004, https://doi.org/10.1029/2005RG000183.

Georgelin, M., and F. Lott, 2001: On the transfer of momentum by trapped lee waves: Case of the IOP 3 of PYREX. *J. Atmos. Sci.*, **58**, 3563–3580, https://doi.org/10.1175/1520-0469(2001)058<3563:OTTOMB>2.0.CO;2.

Gerbier, N., and M. Berenger, 1961: Experimental studies of lee waves in the French Alps. *Quart. J. Roy. Meteor. Soc.*, **87**, 13–23, https://doi.org/10.1002/qj.49708737103.

Grisogono, B., and D. Belusic, 2009: A review of recent advances in understanding the meso- and microscale properties of the severe bora wind. *Tellus*, **61A**, 1–16, https://doi.org/10.1111/j.1600-0870.2008.00369.x.

Grønås, S., and A. D. Sandvik, 1999: Numerical simulations of local winds over steep orography in the storm over north Norway on October 12, 1996. *J. Geophys. Res.*, **104**, 9107–9120, https://doi.org/10.1029/1998JD200115.

Gu, H., J. Jin, Y. Wu, M. B. Ek, and Z. M. Subin, 2015: Calibration and validation of lake surface temperature simulations with the coupled WRF–lake model. *Climatic Change*, **129**, 471–483, https://doi.org/10.1007/s10584-013-0978-y.

Hills, M. O., D. R. Durran, and P. N. Blossey, 2016: The dissipation of trapped lee waves. Part II: The relative importance of the boundary layer and the stratosphere. *J. Atmos. Sci.*, **73**, 943–955, https://doi.org/10.1175/JAS-D-15-0175.1.

Holtslag, A. A. M., and Coauthors, 2013: Stable atmospheric boundary layers and diurnal cycles: Challenges for weather and climate models. *Bull. Amer. Meteor. Soc.*, **94**, 1691–1706, https://doi.org/10.1175/BAMS-D-11-00187.1.

Iacono, M. J., J. S. Delamere, E. J. Mlawer, M. W. Shephard, S. A. Clough, and W. D. Collins, 2008: Radiative forcing by long-lived greenhouse gases: Calculations with the AER radiative transfer models. *J. Geophys. Res.*, **113**, D13103, https://doi.org/10.1029/2008JD009944.

Jiang, Q., and J. D. Doyle, 2004: Gravity wave breaking over the central Alps: Role of complex terrain. *J. Atmos. Sci.*, **61**, 2249–2266, https://doi.org/10.1175/1520-0469(2004)061<2249:GWBOTC>2.0.CO;2.

——, ——, and R. B. Smith, 2006: Interaction between trapped waves and boundary layers. *J. Atmos. Sci.*, **63**, 617–633, https://doi.org/10.1175/JAS3640.1.

Jiménez, P. A., J. F. González-Rouco, E. García-Bustamante, J. Navarro, J. P. Montávez, J. V. de Arellano, J. Dudhia, and A. Muñoz-Roldan, 2010: Surface wind regionalization over complex terrain: Evaluation and analysis of a high-resolution WRF simulation. *J. Appl. Meteor. Climatol.*, **49**, 268–287, https://doi.org/10.1175/2009JAMC2175.1.

Kain, J. S., 2004: The Kain–Fritsch convective parameterization: An update. *J. Appl. Meteor.*, **43**, 170–181, https://doi.org/10.1175/1520-0450(2004)043<0170:TKCPAU>2.0.CO;2.

Kirshbaum, D. J., 2017: On upstream blocking over heated mountain ridges. *Quart. J. Roy. Meteor. Soc.*, **143**, 53–68, https://doi.org/10.1002/qj.2945.

Klemp, J. B., and D. K. Lilly, 1978: Numerical simulation of hydrostatic mountain waves. *J. Atmos. Sci.*, **35**, 78–107, https://doi.org/10.1175/1520-0469(1978)035<0078:NSOHMW>2.0.CO;2.

Li, L., and Y. Chen, 2017: Numerical simulations of two trapped mountain lee waves downstream of Oahu. *J. Appl. Meteor. Climatol.*, **56**, 1305–1324, https://doi.org/10.1175/JAMC-D-15-0341.1.

Lim, K. S. S., and S. Y. Hong, 2010: Development of an effective double-moment cloud microphysics scheme with prognostic cloud condensation nuclei (CCN) for weather and climate models. *Mon. Wea. Rev.*, **138**, 1587–1612, https://doi.org/10.1175/2009MWR2968.1.

Liu, Y., and Coauthors, 2011: Simultaneous nested modeling from the synoptic scale to the LES scale for wind energy applications. *J. Wind Eng. Ind. Aerodyn.*, **99**, 308–319, https://doi.org/10.1016/j.jweia.2011.01.013.

Long, R. R., 1953: Some aspects of the flow of stratified fluids. I. A theoretical investigation. *Tellus*, **5**, 42–58, https://doi.org/10.3402/tellusa.v5i1.8563.

——, 1955: Some aspects of the flow of stratified flows. III. Continuous density gradients. *Tellus*, **7**, 341–357, https://doi.org/10.3402/tellusa.v7i3.8900.

Lott, F., 2016: A new theory for downslope windstorms and trapped mountain waves. *J. Atmos. Sci.*, **73**, 3585–3597, https://doi.org/10.1175/JAS-D-15-0342.1.

——, and M. J. Miller, 1997: A new subgrid-scale orographic drag parameterization: Its formulation and testing. *Quart. J. Roy. Meteor. Soc.*, **123**, 101–127, https://doi.org/10.1002/qj.49712353704.

Mitchell, R. M., R. P. Cechet, P. J. Turner, and C. C. Elsum, 1990: Observation and interpretation of wave clouds over Macquarie Island. *Quart. J. Roy. Meteor. Soc.*, **116**, 741–752, https://doi.org/10.1002/qj.49711649310.

Mobbs, S. D., and Coauthors, 2005: Observations of downslope winds and rotors in the Falkland Islands. *Quart. J. Roy. Meteor. Soc.*, **131**, 329–351, https://doi.org/10.1256/qj.04.51.

Muñoz-Esparza, D., B. Kosović, J. Mirocha, and J. van Beeck, 2014: Bridging the transition from mesoscale to microscale turbulence in numerical weather prediction models. *Bound.-Layer Meteor.*, **153**, 409–440, https://doi.org/10.1007/s10546-014-9956-9.

——, J. K. Lundquist, J. A. Sauer, B. Kosović, and R. R. Linn, 2017: Coupled mesoscale-LES modeling of a diurnal cycle during the CWEX-13 field campaign: From weather to boundary-layer eddies. *J. Adv. Model. Earth Syst.*, **9**, 1572–1594, https://doi.org/10.1002/2017MS000960.

Ólafsson, H., and H. Ágústsson, 2007: The Freysnes downslope windstorm. *Meteor. Z.*, **16**, 123–130, https://doi.org/10.1127/0941-2948/2007/0180.

Pearce, R. P., and P. W. White, 1967: Lee wave characteristics derived from a three-layer model. *Quart. J. Roy. Meteor. Soc.*, **93**, 155–165, https://doi.org/10.1002/qj.49709339602.

Phillips, T. J., and P. J. Gleckler, 2006: Evaluation of continental precipitation in 20th century climate simulations: The utility of multimodel statistics. *Water Resour. Res.*, **42**, 446–455, https://doi.org/10.1029/2005WR004313.

Pokharel, B., B. Geerts, X. Chu, and P. Bergmaier, 2017: Profiling radar observations and numerical simulations of a persistent downslope windstorm and rotor on the lee of the Medicine Bow Mountains, Wyoming. *Atmosphere*, **8**, 39, https://doi.org/10.3390/atmos8020039.

Ralph, F. M., and P. J. Neiman, 1997: Observations, simulations, and analysis of nonstationary trapped lee waves. *J. Atmos. Sci.*, **54**, 1308–1333, https://doi.org/10.1175/1520-0469(1997)054<1308:OSAAON>2.0.CO;2.

Reinecke, P. A., and D. R. Durran, 2008: Estimating topographic blocking using a Froude number when the static stability is nonuniform. *J. Atmos. Sci.*, **65**, 1035–1048, https://doi.org/10.1175/2007JAS2100.1.

Rögnvaldsson, Ó., J.-W. Bao, H. Ágústsson, and H. Ólafsson, 2011: Downslope windstorm in Iceland–WRF/MM5 model comparison. *Atmos. Chem. Phys.*, **11**, 103–120, https://doi.org/10.5194/acp-11-103-2011.

Sachsperger, J., S. Serafin, V. Grubišić, I. Stiperski, and A. Paci, 2017: The amplitude of lee waves on the boundary-layer inversion. *Quart. J. Roy. Meteor. Soc.*, **143**, 27–36, https://doi.org/10.1002/qj.2915.

Sauer, J. A., D. Muñoz-Esparza, J. M. Canfield, K. R. Costigan, R. R. Linn, and Y. Kim, 2016: A large-eddy simulation study of atmospheric boundary layer influence on stratified flows over terrain. *J. Atmos. Sci.*, **73**, 2615–2632, https://doi.org/10.1175/JAS-D-15-0282.1.

Sawyer, J. S., 1960: Numerical calculation of the displacements of a stratified airstream crossing a ridge of small height. *Quart. J. Roy. Meteor. Soc.*, **86**, 326–345, https://doi.org/10.1002/qj.49708636905.

Scorer, R. S., 1949: Theory of waves in the lee of mountains. *Quart. J. Roy. Meteor. Soc.*, **75**, 41–56, https://doi.org/10.1002/qj.49707532308.

——, and H. Klieforth, 1959: Theory of mountain waves of large amplitude. *Quart. J. Roy. Meteor. Soc.*, **85**, 131–143, https://doi.org/10.1002/qj.49708536406.

Sheridan, P. F., and S. B. Vosper, 2006: A flow regime diagram for forecasting lee waves, rotors, and downslope winds. *Meteor. Appl.*, **13**, 179–195, https://doi.org/10.1017/S1350482706002088.

Shi, X., Y. Wang, and X. Xu, 2008: Effect of mesoscale topography over the Tibetan Plateau on summer precipitation in China: A regional model study. *Geophys. Res. Lett.*, **35**, L19707, https://doi.org/10.1029/2008GL034740.

Shi, Z., Y. Sha, and X. Liu, 2017: Effect of Yunnan–Guizhou topography at the southeastern Tibetan Plateau on the Indian monsoon. *J. Climate*, **30**, 1259–1272, https://doi.org/10.1175/JCLI-D-16-0105.1.

Shin, H. H., and S. Y. Hong, 2011: Intercomparison of planetary boundary-layer parametrizations in the WRF Model for a single day from CASES-99. *Bound.-Layer Meteor.*, **139**, 261–281, https://doi.org/10.1007/s10546-010-9583-z.

——, and ——, 2015: Representation of the subgrid-scale turbulent transport in convective boundary layers at gray-zone resolutions. *Mon. Wea. Rev.*, **143**, 250–271, https://doi.org/10.1175/MWR-D-14-00116.1.

Skamarock W. C., and Coauthors, 2008: A description of the Advanced Research WRF version 3. NCAR Tech. Note NCAR/TN-475+STR, 113 pp., https://doi.org/10.5065/D68S4MVH.

Smith, R. B., 2007: Interacting mountain waves and boundary layers. *J. Atmos. Sci.*, **64**, 594–607, https://doi.org/10.1175/JAS3836.1.

——, J. D. Doyle, Q. Jiang, and S. A. Smith, 2007: Alpine gravity waves: Lessons from MAP regarding mountain wave generation and breaking. *Quart. J. Roy. Meteor. Soc.*, **133**, 917–936, https://doi.org/10.1002/qj.103.

Smith, S. A., J. D. Doyle, A. R. Brown, and S. Webster, 2006: Sensitivity of resolved mountain drag to model resolution for MAP case-studies. *Quart. J. Roy. Meteor. Soc.*, **132**, 1467–1487, https://doi.org/10.1256/qj.05.67.

Talbot, C., E. Bou-Zeid, and J. Smith, 2012: Nested mesoscale large-eddy simulations with WRF: Performance in real test cases. *J. Hydrometeor.*, **13**, 1421–1441, https://doi.org/10.1175/JHM-D-11-048.1.

Teixeira, J., and Coauthors, 2008: Parameterization of the atmospheric boundary layer: a view from just above the inversion. *Bull. Amer. Meteor. Soc.*, **89**, 453–458, https://doi.org/10.1175/BAMS-89-4-453.

Udina, M., M. R. Soler, and O. Sol, 2017: A modeling study of a trapped lee-wave event over the Pyrénées. *Mon. Wea. Rev.*, **145**, 75–96, https://doi.org/10.1175/MWR-D-16-0031.1.

van Stratum, B. J. H., and B. Stevens, 2015: The influence of misrepresenting the nocturnal boundary layer on idealized daytime convection in large-eddy simulation. *J. Adv. Model. Earth Syst.*, **7**, 423–436, https://doi.org/10.1002/2014MS000370.

Vergeiner, I., and D. K. Lilly, 1970: The dynamic structure of lee wave flow as obtained from balloon and airplane observations. *Mon. Wea. Rev.*, **98**, 220–232, https://doi.org/10.1175/1520-0493(1970)098<0220:TDSOLW>2.3.CO;2.

von Storch, H., 1995: Inconsistencies at the interface of climate impact studies and global climate research. *Meteor. Z.*, **4**, 72–80, https://doi.org/10.1127/metz/4/1992/72.

Vosper, S. B., 2004: Inversion effects on mountain lee waves. *Quart. J. Roy. Meteor. Soc.*, **130**, 1723–1748, https://doi.org/10.1256/qj.03.63.

Wang, C., J. Wang, Z.-L. Zhang, and D.-Y. Guo, 2010: Effects of wind field on lee wave in three-layer model. *J. Meteor. Environ.*, **26**, 66–71.

Wyngaard, J. C., 2004: Toward numerical modeling in the "terra incognita." *J. Atmos. Sci.*, **61**, 1816–1826, https://doi.org/10.1175/1520-0469(2004)061<1816:TNMITT>2.0.CO;2.

Yang, C., Z. Fu, and X. Zhao, 2013: Analysis of climatic characteristics of gales in complex topographic area. *30th Annual Meeting of the Chinese Meteorological Society*, Nanjing, China, Chinese Meteorological Society, P458, 10 pp.

——, ——, and ——, 2014: Diagnostic analysis of winter gale complex terrain in the southeast of Qinghai-Xizang Plateau. *Plateau Meteor.*, **33**, 346–354.

Zang, Z.-L., M. Zhang, and H. Huang, 2007: Influence of the Scorer parameter profile on the wavelength of trapped lee waves. *J. Hydrodyn.*, **19**, 165–172, https://doi.org/10.1016/S1001-6058(07)60044-4.

——, and ——, 2008: A study of the environmental influence on the amplitude of lee waves. *Adv. Atmos. Sci.*, **25**, 474, https://doi.org/10.1007/s00376-008-0474-x.

Zhang, R., T. Koike, X. Xu, Y. Ma, and K. Yang, 2012: A China-Japan cooperative JICA atmospheric observing network over the Tibetan Plateau (JICA/Tibet Project): An overviews. *J. Meteor. Soc. Japan*, **90C**, 1–16, https://doi.org/10.2151/jmsj.2012-C01.

Zhao, P., and Coauthors, 2018: The third atmospheric scientific experiment for understanding the Earth–atmosphere coupled system over the Tibetan Plateau and its effects. *Bull. Amer. Meteor. Soc.*, **99**, 757–776, https://doi.org/10.1175/BAMS-D-16-0050.1.

Zhou, B., and F. K. Chow, 2013: Nighttime turbulent events in a steep valley: A nested large eddy simulation study. *J. Atmos. Sci.*, **70**, 3262–3276, https://doi.org/10.1175/JAS-D-13-02.1.

Zhu, P., 2008: A multiple scale modeling system for coastal hurricane wind damage mitigation. *Nat. Hazards*, **47**, 577–591, https://doi.org/10.1007/s11069-008-9240-8.